Phase separation of self-propelled disks with ferromagnetic and nematic alignment

Elena Sesé-Sansa,[1,*] Demian Levis,[2,3] and Ignacio Pagonabarraga[1,2,3]

[1]*CECAM, Centre Européen de Calcul Atomique et Moléculaire, Ecole Polytechnique Fédérale de Lausanne (EPFL), Batochime, Avenue Forel 2, 1015 Lausanne, Switzerland*

[2]*Departament de Física de la Matèria Condensada, Universitat de Barcelona, Martí i Franquès 1, 08028 Barcelona, Spain*

[3]*UBICS University of Barcelona Institute of Complex Systems, Martí i Franquès 1, E08028 Barcelona, Spain*

(Received 16 June 2021; accepted 25 October 2021; published 18 November 2021)

We present a comprehensive study of a model system of repulsive self-propelled disks in two dimensions with ferromagnetic and nematic velocity alignment interactions. We characterize the phase behavior of the system as a function of the alignment and self-propulsion strength, featuring orientational order for strong alignment and motility-induced phase separation (MIPS) at moderate alignment but high enough self-propulsion. We derive a microscopic theory for these systems yielding a closed set of hydrodynamic equations from which we perform a linear stability analysis of the homogenous disordered state. This analysis predicts MIPS in the presence of aligning torques. The nature of the continuum theory allows for an explicit quantitative comparison with particle-based simulations, which consistently shows that ferromagnetic alignment fosters phase separation, while nematic alignment does not alter either the nature or the location of the instability responsible for it. In the ferromagnetic case, such behavior is due to an increase of the imbalance of the number of particle collisions along different orientations, giving rise to the self-trapping of particles along their self-propulsion direction. On the contrary, the anisotropy of the pair correlation function, which encodes this self-trapping effect, is not significantly affected by nematic torques. Our work shows the predictive power of such microscopic theories to describe complex active matter systems with different interaction symmetries and sheds light on the impact of velocity-alignment interactions in motility-induced phase separation.

DOI: 10.1103/PhysRevE.104.054611

I. INTRODUCTION

Inspired by living organisms, active matter made of self-propelled units comprises a wide variety of systems whose common feature is the continuous consumption of energy converted into directed motion. Several well-known examples of active systems can be found in the biological world as well as synthetically realized in manmade systems across scales [1]: examples range from flocks of birds [2], bacteria [3–6], cells [7–9], or cytoskeletal components [10–13] to self-propelled colloids [14–16] or grains [17–19]. One of the main interests of these systems lies in the fact that, since they are intrinsically out-of-equilibrium and host different kinds of complex interactions, they display a wide range of emergent collective phenomena. For instance, particle's aggregation in the absence of attractive interactions [14,16,20–22] and the emergence of collective motion [3,4,10,17,22] are among the most salient examples.

The description of these nonequilibrium phenomena has attracted a great deal of theoretical work over the last decades [23,24]. Much progress has been achieved through the study of minimal models capturing some key, hopefully generic, features of active systems. Among them, so-called "dry models" have played (and are still playing) an important role in the development of a theoretical framework to understand and classify different collective behavior observed in active systems [25,26]. Dry models, as their name suggests, neglect the role played by the surrounding medium hosting these self-propelled components, besides as a source of fluctuations and dissipation. They are based on minimal symmetry and dimensionality considerations, following a trend of ideas surely inspired by the theory of critical phenomena. Following the symmetry of their constituents, dry models can be classified in different universality classes. For active matter, however, an extra ingredient with no equivalent in the theory of equilibrium critical phenomena has to be taken into account: the symmetry associated to the self-propulsion mechanism itself. In this work, we focus on particles carrying an orientation which sets their self-propulsion direction. Thus, since one can associate an "arrow" to each particle, they are said to be *polar*. On top of that, one has to consider, as usual, the symmetry of their interactions.

A natural, and extensively studied, class of active systems made of polar self-propelled particles is the one defined by *isotropic* particle-particle interactions. This encompasses the active Brownian particle (ABP) model [27–29], which describes agents performing a persistent walk and interacting solely through volume-exclusion (as illustrated in the first column Fig. 1). Together with its coarse-grained theories [30–37], this class of models describes the aggregation of self-propelled particles in the absence of attractions, resulting in a macroscopic phase separation at high enough density and

*elena.sesesansa@epfl.ch

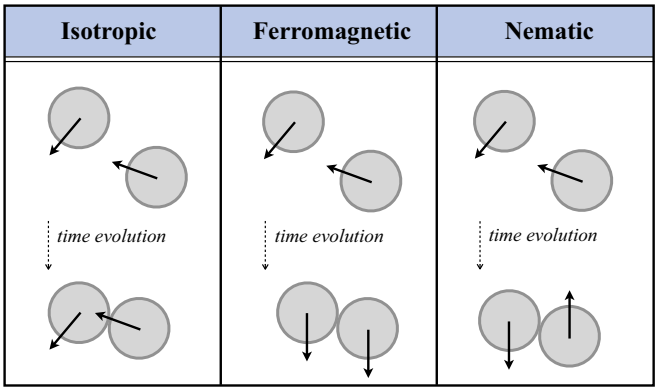

FIG. 1. Schematic representation of our model system, comprising active Brownian particles subjected to (i) only isotropic excluded volume interactions (first column), (ii) ferromagnetic velocity-alignment (second column), and (iii) nematic velocity-alignment (third column).

self-propulsion strength: the so-called motility-induced phase separation (MIPS) [38–49].

The arguably most studied and first introduced "universality class" in active matter is the one that considers *ferromagnetic* (or polar) interactions, meaning, particles that locally align their velocity with the one of their neighbors. The celebrated Vicsek model [50] and its continuous descriptions pioneered by Toner and Tu [51], describing the emergence of collective motion, belong to this class (second column Fig. 1).

Many extensions of the Vicsek model have been considered, accounting for different kinds of alignment rules [25]. In particular, the case in which particles align along a preferred axis with head-tail *nematic* symmetry has received considerable attention [52–55], as being models of self-propelled elongated objects, such as most swimming bacteria (third column Fig. 1). This class of active systems is typically referred to as *active rods* [56], both for self-propelled particles with an alignment rule à la Vicsek, and for rigid elongated objects for which nematic alignment results from collisions, i.e., anisotropic excluded volume interactions [57–63]. Despite sharing the same nomenclature, self-propelled rods interacting via volume exclusion feature different emergent states than the simplified polar point-like particles with nematic alignment. They can, for instance, form coherently moving polar clusters while Vicsek-like particles cannot, and their aspect ratio turns out to be a crucial parameter as it allows them to go from an alignment dominated regime, to an isotropic regime exhibiting MIPS.

Here, we investigate the interplay between excluded volume and velocity alignment. Most recent studies addressing this problem focus on the role played by the particles' shape in the emergence of different states, mainly looking at how MIPS destabilizes in favor of oriented structures [60–63]. To disentangle the role played by each one of these two interaction mechanisms, short-range repulsion and alignment, we consider a system of self-propelled particles with isotropic excluded volume interactions but anisotropic aligning torques, both of ferromagnetic and nematic nature, as illustrated in Fig. 1. In other words, we aim at understanding (i) how (isotropic) excluded volume interactions affect the collective behavior of the ferromagnetic and nematic Vicsek-like class of systems, without interfering with more complex aspects related to the shape of the particles and (ii) how ferromagnetic and nematic alignment affect the MIPS of self-propelled disks. Such questions have recently been addressed for ferromagnetic [22,64–70], nematic [71], and other kinds of more complex aligning mechanisms present in colloidal experiments [72]. However, a unified framework allowing to unravel the impact of aligning torques with different symmetries on the phase behavior of ABP is still lacking.

The paper is organized as follows. In Sec. II, we introduce a microscopic ABP model combining excluded volume and velocity alignment interactions. In Sec. III, we discuss the phase diagram of the system subjected to either ferromagnetic or nematic alignment obtained from Brownian dynamics simulations. In Sec. IV, we systematically derive a continuum description by explicitly coarse-graining the stochastic particle dynamics. We then perform a linear stability analysis of the resulting effective hydrodynamic equations, focusing on the stability of the homogeneous isotropic state. Finally, we compare the numerical results to the predictions of the analysis of the continuum equations and discuss how a ferromagnetic and a nematic coupling affect the phase separation of repulsive self-propelled disks.

II. MICROSCOPIC ABP MODEL

We consider a 2D system of N particles in a $L\times L$ box with periodic boundary conditions at positions $\mathbf{r}_i$ and with orientations $\mathbf{e}_i = (\cos\varphi_i, \sin\varphi_i)$, whose dynamics are governed by the set of coupled over-damped Langevin equations:

$$\dot{\mathbf{r}}_i(t) = v_0\mathbf{e}_i + \mu\mathbf{F}_i(\{r_j(t)\}) + \sqrt{2D_0}\boldsymbol{\eta}_i(t), \tag{1}$$

$$\dot{\varphi}_i(t) = -\mu_r\frac{\partial\mathcal{H}}{\partial\varphi_i} + \sqrt{2D_r}\nu_i(t). \tag{2}$$

Particles self-propel at constant speed v_0 in the direction given by $\mathbf{e}_i$. The time evolution of $\mathbf{e}_i$ is subjected to local torques $T_i = -\frac{\partial\mathcal{H}}{\partial\varphi_i}$ which derive from a Vicsek-like alignment rule that we specify below. Particles also interact through isotropic, short-range, repulsive forces, $\mathbf{F}_i$. The system is in contact with a thermal bath, modeled by $\boldsymbol{\eta}_i$, a Gaussian white noise with zero mean and unit variance. Orientations are subjected to rotational noise, ν_i, also described by a Gaussian white noise with zero mean and unit variance. Rotational noise sets a characteristic time scale, given by the inverse of the rotational diffusion coefficient, $\tau_r = D_r^{-1}$, the persistence time, and a characteristic length scale given by $l_p = v_0\tau_r$, the persistence length. The thermal diffusion coefficient D_0 and the mobility μ fulfill the Einstein relation $D_0 = \mu k_B T$, where k_B is the Boltzmann constant and T the temperature of the bath.

We now specify the different interaction terms, included in our model equations Eqs. (1) and (2) and used in the present work.

A. Excluded volume

The excluded volume interaction, $\mathbf{F}_i = -\sum_{j\neq i} \nabla_i u(r_{ij})$, derives from a WCA potential,

$$u(r_{ij}) = \begin{cases} 4u_0\left[\left(\frac{\sigma}{r_{ij}}\right)^{12} - \left(\frac{\sigma}{r_{ij}}\right)^{6}\right] + u_0 & r_{ij} \leqslant R, \\ 0 & r_{ij} > R, \end{cases} \tag{3}$$

where $r_{ij} = |\mathbf{r}_i - \mathbf{r}_j|$. The cutoff distance is $R = 2^{1/6}\sigma$ and u_0 corresponds to the characteristic energy scale of the potential.

B. Aligning torques

Local torques derive from the following Hamiltonian (potential)

$$\mathcal{H} = -\sum_{i,j} v(r_{ij}) w(\varphi_{ij}), \tag{4}$$

where $\varphi_{ij} = \varphi_i - \varphi_j$ and

$$v(r_{ij}) = \begin{cases} \frac{2}{\pi R_\varphi^2}(r_{ij} - R_\varphi)^2 & r_{ij} < R_\varphi \\ 0 & r_{ij} > R_\varphi \end{cases} \tag{5}$$

is a spatially decaying function with a cutoff distance R_φ, setting the interaction range beyond which particles do not align. The spatial dependency of $v(r_{ij})$ ensures that there are no discontinuities in the resulting torque. The angular dependency of the alignment potential, $w(\varphi_{ij})$, is chosen in different ways to study interactions of different nature: (a) ferromagnetic and (b) nematic alignment.

In the absence of alignment interactions, the model described by Eqs. (1) and (2) reduces to the Active Brownian Particle model. In this limit, the system undergoes motility-induced phase separation upon increasing the self-propulsion speed. Furthermore, in the absence of excluded volume interactions, $u_0 = 0$, the model describes pointlike particles *à la* Vicsek, subjected to alignment interactions of different nature.

1. Ferromagnetic alignment

Ferromagnetic torques lead to a Langevin variant (in continuous time) of the Vicsek model, which, in the limit of vanishing velocities reduces to the equilibrium 2D XY model of a ferromagnet. Indeed, a ferromagnetic coupling in Eq. (2) can be derived from the 2D XY Hamiltonian

$$\mathcal{H} = -J \sum_i \sum_{j\in\omega_i} v(r_{ij})\, \mathbf{e}_i \cdot \mathbf{e}_j, \tag{6}$$

meaning

$$w(\varphi_{ij}) = J\cos(\varphi_{ij}), \tag{7}$$

where ω_i is the vicinity of particle i, defined by R_φ, and $J > 0$ is the coupling strength.

2. Nematic alignment

Nematic torques tend to align the direction of self-propulsion of neighboring particles along the same axis but with no head-tail preference, see Fig. 1, in the same fashion as uniaxial nematic liquid crystals [73]. Thus, the nematic interaction can be modeled by the following Hamiltonian:

$$\mathcal{H} = -J \sum_i \sum_{j\in\omega_i} v(r_{ij})\, \mathbf{q}_i \cdot \mathbf{q}_j, \tag{8}$$

where $\mathbf{q}_i = \mathbf{e}_i \otimes \mathbf{e}_i - \frac{1}{2}\mathbb{1}$ is the nematic tensor [74]. Note that Eq. (8) has the same structure as the 2D XY model interaction, but now the nematic tensor plays the role of the orientation of the particles (spins) [75]. From such Hamiltonian one gets (see Appendix A)

$$w(\varphi_{ij}) = J\cos(2\varphi_{ij}). \tag{9}$$

At this stage, it is possible to identify the relevant set of dimensionless parameters: the average packing fraction

$$\phi = \frac{N\pi R^2}{4L^2} \equiv \overline{\rho}\frac{\pi R^2}{4}, \tag{10}$$

the reduced coupling parameter

$$g = \frac{2\mu_r J}{\pi R_\varphi^2 D_r}, \tag{11}$$

accounting for the strength of the alignment interaction as compared to the rotational diffusion, and the Péclet number

$$\mathrm{Pe} = \frac{v_0}{RD_r} = l_p/R, \tag{12}$$

quantifying the persistence of the particle's motion.

We systematically study the system's phase behavior fixing $\phi = 0.4$ and varying g and Pe. To this end, we perform Brownian dynamics simulations of the model described in Eqs. (1) and (2) with $N = 4000$–$16\,000$ particles in a $L\times L$ box subjected to periodic boundary conditions (PBC). The steric interaction cutoff distance is set to $R = 1$, which in turn gives the unit of length (interpreted as the effective diameter of the particles). The strength of the pairwise repulsive interaction is $u_0 = 100$, in units of the thermal energy, $k_BT = 1$. The time unit is given by $\tau_0 = R^2/D_0 = 1$, where the thermal diffusion coefficient is $D_0 = R^2D_r/3$, with fixed rotational diffusion coefficient $D_r = 3/\tau_0$. This, in turn, sets the characteristic decorrelation time, $\tau_r = D_r^{-1}$. The alignment cutoff distance is set to $R_\varphi = 2R$, so that particles need not be in contact to mutually align their directions of self-propulsion. We explore a range of v_0 values that goes from 0 to 400, corresponding to Pe $\in [0, 133.3]$. The coupling constant J takes values from 0 to 320 and thus $g \in [0, 17.0]$. Finally, mobilities are set to $\mu = \mu_r = 1$.

The simulations are performed by initializing the system in a random configuration and letting it relax to its steady state. The results reported are obtained by averaging over ensembles of 1000 independent configurations at the stationary state (in the regime of low Pe where density and polarization fluctuations are bigger, we sample systems of $N = 8000$ and average over 5000 independent configurations). We use an Euler-Mayurama algorithm to integrate the equations of motion. The timestep employed to discretize the equations of motion ranges from $\Delta t = 10^{-5}$ to $\Delta t = 2\times10^{-6}$, depending on the value of Pe. Each simulation lasts for $320\tau_r$, in terms of the decorrelation time τ_r. Initially, we let the system evolve for $120\tau_r$, until it reaches the steady state, and then record a configuration every $2\tau_r$ for further statistical analysis. We explored by means of numerical simulations the behavior of the system by varying g and Pe, subjected to either ferromagnetic or nematic alignment at fixed $\phi = 0.4$. The resulting state diagram obtained for systems with $N = 4000$ is shown in

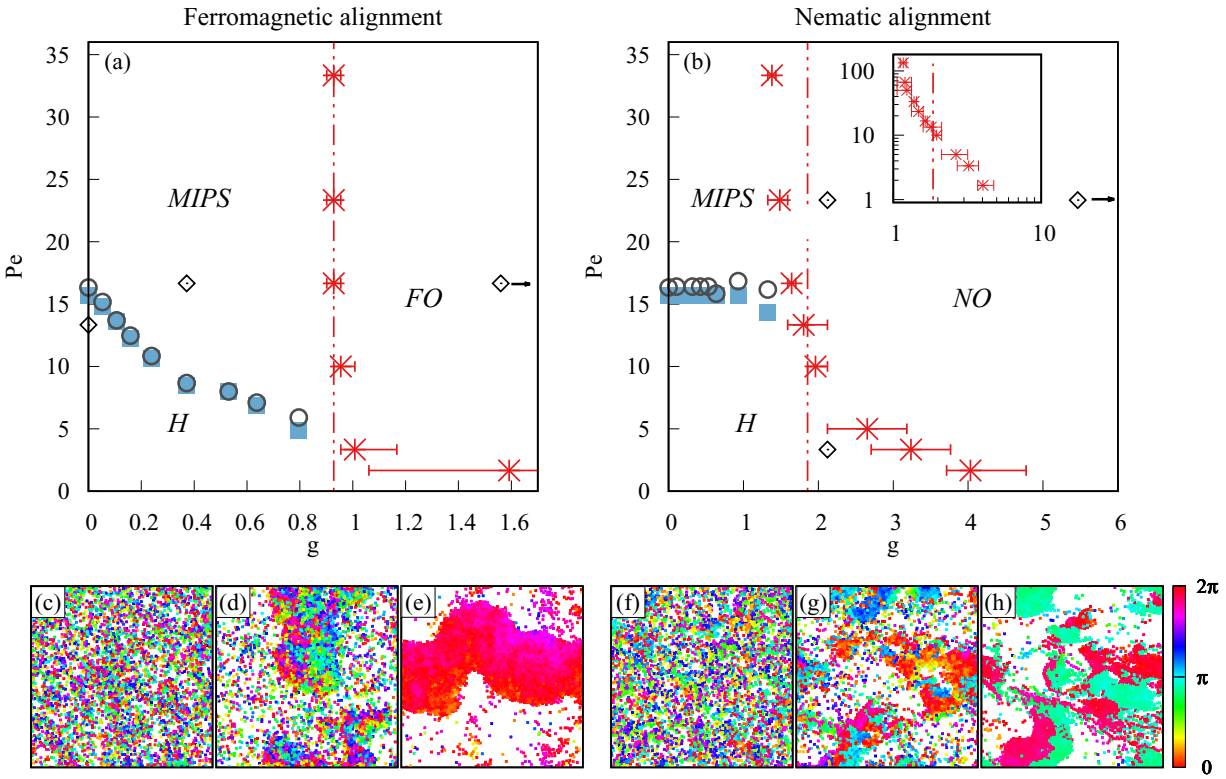

FIG. 2. Phase diagram in the (g, Pe) plane for a system at $\phi = 0.4$ with (a) local ferromagnetic alignment and (b) local nematic alignment. The phase separation from a homogeneous (H) to a MIPS state is indicated by blue squares. The prediction of the phase separation given by the continuum theory is marked by grey circles. The onset of ferromagnetic order (FO) and nematic order (NO) is marked by red symbols with error bars. The inset in panel (b) shows the onset of nematic order up to a value of Pe = 133.4 in log-log scale. Broken lines correspond to $g = g_f = 0.93$ in panel (a) and $g = 2g_f$ in panel (b). Snapshots of the system at different points of the phase diagrams (indicated by symbols) (c) (0, 13.3); (d) (0.37, 16.6); (e) (7.96, 16.6) in the ferromagnetic case; (f) (2.12, 3.3); (g) (2.12, 23.4); (h) (13.23, 23.4) in the nematic case. Particles are colored according to their self-propulsion direction, using a cyclic color code. Particles with the same color share the same orientation.

Fig. 2. Aligning torques induce the emergence of orientational order in the system, either of ferromagnetic or nematic nature, while the competition between self-propulsion and excluded volume interactions triggers phase separation. The study of the latter in the presence of aligning interactions is the main object of the present article and presented in Secs. IV and V.

III. PHASE BEHAVIOR

A. Emergence of orientational order

Upon increasing the tendency of particles to align at fixed self-propulsion velocity, the system undergoes a phase transition between an isotropic and an oriented state (see snapshots in Fig. 2). At low values of the coupling parameter, the orientational dynamics of particles is dominated by rotational noise, thus leading to a disordered state. Upon increasing g, local alignment torques overcome rotational noise and eventually trigger the emergence of global orientational order. A macroscopic fraction of the particles in this state is thus aligned, leading to the emergence of collective motion (or flocking), Figs. 2(e) and 2(h).

Obviously, the nature of the ordered phases strongly depends on the symmetry of the alignment interactions. For ferromagnetic alignment, the ordered state displays polar order and strong density heterogeneities in the form of lanes, as illustrated in Fig. 2(e), along which a macroscopic fraction of the system moves (roughly) along the same direction. The formation of dense structures such as traveling bands are typical in flocking Vicsek-style models [25]. Extensions of such models including volume interactions display richer structures, and among them, it is typical to find lanes [64,65,67].

Local nematic torques lead, instead, to an ordered state where particles self-propel along the same axis but in opposite directions, Fig. 2(h). Here, the ordered phase is also characterized by the formation of dense structures, although of different nature than in the ferromagnetic case. Particles with nematic alignment aggregate into coherently-moving structures, with a high degree of local polar order. These domains collide and interpenetrate, giving rise to elongated, nematically ordered structures that we call, by extension of Vicsek-type models, nematic bands. An illustration of these nematic bands is provided by the snapshots Figs. 2(g)–2(h). While nematic bands are generically found in Vicsek-type models of active rods [25], the situation becomes quite more intricate when excluded volume interactions are considered. In active rod models, made of elongated self-propelled particles that align through collisions, one generically observes the formation of polar lanes, similar to the ones we observe in the ferromagnetic case, at high enough densities and shape anisotropy [58,60,62,63]. Here, we also find a tendency towards polar

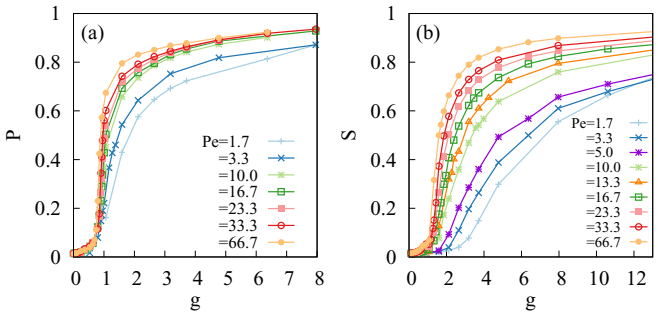

FIG. 3. (a) Global polarization as a function of the normalized ferromagnetic alignment strength for different values of the self-propulsion speed; (b) global nematic order as a function of the normalized nematic alignment strength.

ordering, however, only locally. The isotropic shape of our particles does not allow for the establishment of a large-scale polar structure even for very strong coupling.

The emergence of ferromagnetic order is characterized by a nonzero value of the polarization

$$P = \left| \frac{1}{N} \sum_{i=1}^{N} \mathbf{e}_i \right|, \tag{13}$$

while nematic order is quantified by the scalar nematic order parameter S [76], defined as

$$S = \frac{2}{N} \left[\left(\sum_i \cos^2 \varphi_i - \frac{1}{2} \right)^2 + \left(\sum_i \cos \varphi_i \sin \varphi_i \right)^2 \right]^{\frac{1}{2}}. \tag{14}$$

The evolution of the averaged order parameters as a function of the coupling strength is shown in Figs. 3(a) and 3(b) in the ferromagnetic and nematic case, respectively. To locate the onset of global ferromagnetic order shown in red symbols in the phase diagram, Fig. 2(a), we compute the susceptibility $\chi(P) = N(\langle P^2 \rangle - \langle P \rangle^2)$, where $\langle \cdot \rangle$ denotes an ensemble average. In the case of nematic alignment, we observe strong fluctuations in S at low Pe, resulting in a broad susceptibility with an ill-defined peak. However, at high values of Pe, $\chi(S)$ peaks at a value of g corresponding to $S = 0.2$. It is for this reason that we use the latter threshold value as a criterion to locate the onset of nematic order at any value of Pe. The phase diagram Fig. 2(b) shows in red symbols the critical value of g corresponding to $S = 0.2$.

From this analysis, we identify the onset of ferromagnetic order at $g_f = 0.93$. This critical coupling is largely independent of the value of Pe, see Fig. 2(a). The independence of the onset of flocking on Pe has been already reported in numerical simulations [67,68] and mean-field calculations [65], according to which it is located at $g \approx 0.63$.

The onset of nematic order g_n(Pe) has a stronger dependence on the value of Pe for the finite system sizes explored. The higher the Pe is, the lower the alignment strength has to be to trigger nematic order. A Pe-dependence of the onset of nematic order has been recently observed in other simulations of nematically aligning ABP [71]. The parallel analysis of ferromagnetic and nematic interactions we perform here allows us to identify that, as Pe increases, the critical value g_n decreases, first approaching $2g_f$, the value expected in the absence of self-propulsion, and then going below that value at very large Pe, saturating at a value around $g_n(\mathrm{Pe} \gg 1) \approx 1.15$. Note that in this high-Pe regime, the persistence length l_p becomes larger than the linear system size $L = 88.6$, such that large-scale fluctuations are strongly suppressed. Thus, the behavior at high Pe is likely to be strongly affected by finite size effects and controlled by mean-field behavior. For $\mathrm{Pe} > 89$, the persistence length of the particles exceeds the linear size of the box L. Larger system sizes, such that $L/l_p \ll 1$, would be needed to analyze finite size effects in this high activity regime. We however did not attempt to characterize the nature of the orientated state. Above $\mathrm{Pe} = 89$, the observed flocking transition is mean-field like and does not depend anymore on the value of Pe. Instead, for smaller values of Pe, or larger system sizes, the nematic order parameter decays at fixed g for increasing l_p.

It is worth mentioning at this stage that the nature of the ordered state in systems of Vicsek particles with nematic alignment has arouse some debate over the last decade. While it is now clear that true long-range order can arise for ferromagnetic interactions, numerical and analytical results have not convincingly yield a conclusion in this respect for the nematic case [52,77], until very recently [55]. In this latter work, it is shown that very large systems need to be explored to grasp the asymptotic quasi-long-range order nature of the ordered state. Thus, in finite, yet large, systems of linear size smaller than a characteristic length scale (which can be made very large) nematic order appears to be long-range. The location of the threshold reported in Fig. 2 has thus to be taken as a description of the behavior of our finite system, bearing in mind the aim of the present study, which is the understanding of the particle aggregation mechanism in the presence of different kind of aligning interactions. The exploration of the phase diagram presented here responds to the need of setting the parameters for our subsequent study of phase separation, but not as an attempt of establishing the asymptotic behavior of the system in the $N \to \infty$ limit. In the presence of excluded volume interactions though, the nature of the phase transition triggered by nematic interactions in systems of self-propelled particles remains an open challenge. We do not aim at addressing this question here.

B. Phase separation

In the absence of effective torques, $g = 0$, the system undergoes a phase separation from a homogeneous (denoted H) to a phase-separated state (MIPS) by increasing Pe (Fig. 2). At finite g below the emergence of orientational order, there is a region of the phase diagram where the system demixes into a dense region, where particles move slowly, and a dilute region where particles move fast. As shown in Ref. [68] for ferromagnetic alignment, such phase separation can be attributed to the MIPS mechanism, meaning, a fast reduction of the particles velocity with increasing local density.

In what follows, we study the impact of alignment (both ferromagnetic and nematic) on the global phase separation induced by motility. We use the fraction of particles in the largest cluster of the system, Π, as a phenomenological order

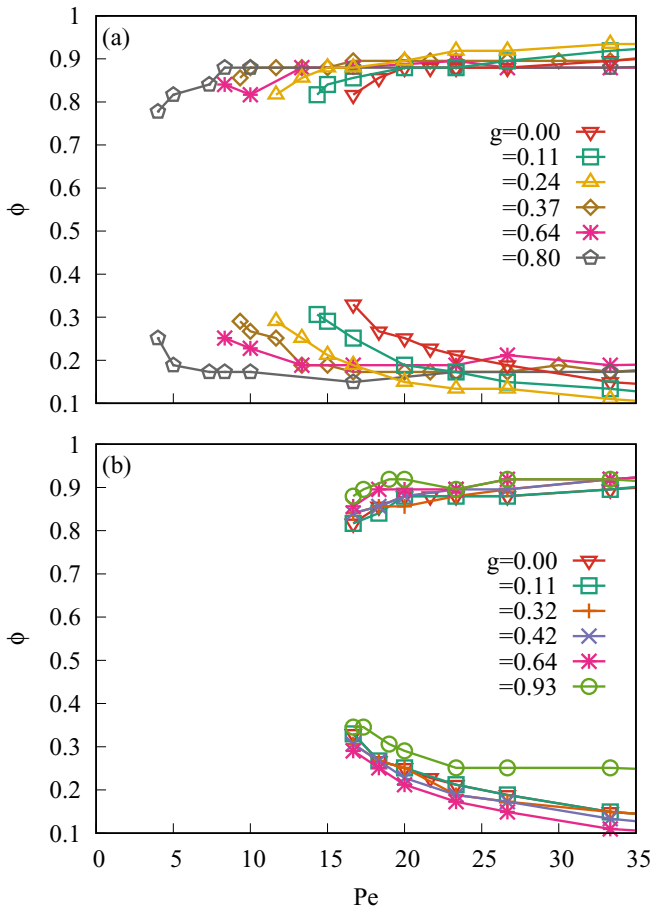

FIG. 4. Phase coexistence regions for several values of the (a) ferromagnetic and (b) nematic alignment strength, g. The coexistence region shifts to lower values of Pe as the ferromagnetic coupling is increased, while increasing the nematic coupling does not significantly affect the coexistence region of nonaligning ABP.

parameter to identify the onset of phase separation (see Appendix B for further details), or spinodal line. We consider the system in a phase separated state when $\Pi > 0.08$ and report the critical value of Pe obtained in this way in the phase diagrams Figs. 2(a) and 2(b).

As shown in Fig. 2(a), for ferromagnetic alignment, MIPS is shifted to lower values of Pe as the coupling parameter g is increased, as reported in Refs. [68,78]. Ferromagnetic alignment enhances the aggregation of particles and the eventual phase separation of the system. In contrast, for nematic alignment, the critical self-propulsion speed at which MIPS takes place remains fairly unchanged as the coupling parameter g is increased, as shown in Fig. 2(b).

To further characterize the effect of different alignment interaction on MIPS, we construct the binodals of the system, shown in Fig. 4, from the analysis of local density distributions. For ferromagnetic alignment, the region of coexistence is shifted to lower values of Pe as g is increased. On the contrary, for nematic alignment, the coexistence regions do not change within our numerical accuracy, in agreement with the results presented in Fig. 2. The MIPS coexistence region of ABP is not significantly affected by the presence of nematic alignment interactions. The system's finite size does not have a strong effect in the MIPS characterization. To show the robustness of the results obtained at $N = 4000$ we have reproduced the binodals for bigger system sizes ($N = 8000, 16\,000$), see Fig. 9 in Appendix C.

With the aim of shedding light on the mechanisms triggering MIPS in the presence of aligning interactions, we develop below a continuum theory by explicitly coarse-graining the microscopic ABP dynamics Eqs. (1) and (2). We then perform a linear stability analysis of the resulting field equations that we can directly compare with our simulation results, thus explaining why ferromagnetic interactions enhance MIPS while nematic ones do not.

IV. COARSE-GRAINED DESCRIPTION

A. Derivation of hydrodynamic equations

The overdamped Langevin dynamics Eqs. (1) and (2) can be equivalently described by the following N-body Smoluchowski equation [30–32,79],

$$\partial_t \psi_N = \sum_{i=1}^{N} \nabla_i \cdot [(\nabla_i U)\psi_N - v_0 \mathbf{e}_i \psi_N + D_0 \nabla_i \psi_N] + \sum_{i=1}^{N} \partial_{\varphi_i}[(\partial_{\varphi_i}\mathcal{H})\psi_N + D_r \partial_{\varphi_i}\psi_N], \tag{15}$$

where $\psi_N(\Gamma = \{\mathbf{r}_i, \varphi_i\}_{i=1..N}, t)$ is the joint probability distribution to find our N particles at a given position with a given orientation at time t. Particles self-propel at constant speed v_0 and are subjected to translational and rotational diffusion. From now on we consider $D_0 = 1$ and drop it in the following expressions. Short-range interactions are modeled by two independent potentials, describing excluded volume and alignment interactions,

$$U(\{\mathbf{r}_j\}) = \sum_{i=1}^{i=N} \sum_{i<j} u(|\mathbf{r}_j - \mathbf{r}_i|),$$
$$\mathcal{H}(\{\mathbf{r}_j\}, \{\varphi_j\}) = \sum_{i<j} v(|\mathbf{r}_j - \mathbf{r}_i|) w(\varphi_j - \varphi_i). \tag{16}$$

Assuming the indistinguishability of particles, it is possible to integrate out $(N-1)$ variables, $\psi_1(\mathbf{r}_1, \varphi_1; t) = N \int_{-\infty}^{\infty} d\mathbf{r}_2 ... d\mathbf{r}_N \int_0^{2\pi} d\varphi_2 ... d\varphi_N \psi_N$, to obtain a Smoluchowski equation for the one-body distribution,

$$\partial_t \psi_1 = -\nabla_1 \cdot [\mathbf{F}(\mathbf{r}_1, \varphi_1; t) + v_0 \mathbf{e}_1 \psi_1 - \nabla_1 \psi_1] - \frac{\partial}{\partial \varphi_1}\left[T(\mathbf{r}_1, \varphi_1; t) - D_r \frac{\partial \psi_1}{\partial \varphi_1}\right]. \tag{17}$$

The effective force reads

$$\mathbf{F}(\mathbf{r}_1, \varphi_1; t) = \int_{-\infty}^{\infty} d\mathbf{r}_2 \int_0^{2\pi} d\varphi_2 u'(r_{12}) \frac{\mathbf{r}_{12}}{r_{12}} \psi_2, \tag{18}$$

and the effective torque corresponds to

$$T(\mathbf{r}_1, \varphi_1; t) = \int_{-\infty}^{\infty} d\mathbf{r}_2 \int_0^{2\pi} d\varphi_2 v(r_{12}) w'(\varphi_{12}) \psi_2, \tag{19}$$

where $\mathbf{r}_{12} = \mathbf{r}_2 - \mathbf{r}_1$ and $\varphi_{12} = \varphi_2 - \varphi_1$. Note that both $\mathbf{F}(\mathbf{r}_1, \varphi_1; t)$ and $T(\mathbf{r}_1, \varphi_1; t)$ depend on the two-body

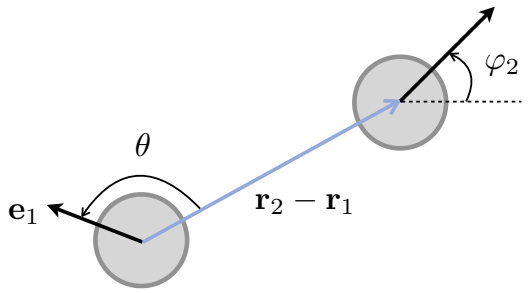

FIG. 5. Schematic representation of two Active Brownian Particles located at $\mathbf{r}_1$ and $\mathbf{r}_2$, setting the notations used throughout the paper. θ is the angle encompassed between the vector distance and the direction of self-propulsion, $\mathbf{e}_1 = (\cos\varphi_1, \sin\varphi_1)$.

probability density, $\psi_2(\mathbf{r}_1, \mathbf{r}_2, \varphi_1, \varphi_2, t)$, and encode the microscopic interactions exerted by the surrounding particles into the tagged particle (labeled *1*). Equation (17) thus constitutes the first equation of a BBGKY-like hierarchy of coupled equations involving multibody distribution functions.

We decompose the two-body probability density using the following identity:

$$\psi_2(\mathbf{r}_1, \mathbf{r}_2, \varphi_1, \varphi_2, t) = \bar{\rho}\,\psi_1(\mathbf{r}_1, \varphi_1, t)\,\mathcal{G}(r_{12}, \theta, \varphi_{12}, t), \quad (20)$$

where $\bar{\rho}$ is the average density, $\mathcal{G}(r_{12}, \theta, \varphi_{12}, t)$ the pair-correlation function and θ the angle encompassed between the vector distance $\mathbf{r}_{12}$ and the orientation of the tagged particle (see sketch in Fig. 5). This decomposition allows us to encode all the information on the microscopic structure of the system in the correlation function $\mathcal{G}(r_{12}, \theta, \varphi_{12}, t)$, interpreted as the probability of finding a particle with orientation φ_2 in the plane-direction θ, at a distance $r_{12} = |\mathbf{r}_{12}|$ from the tagged particle (at $\mathbf{r}_1$ with orientation φ_1, see Fig. 5). From now on, we drop the subscripts for clarity.

We then insert the two-body probability density decomposition Eq. (20) in Eqs. (18) and (19), and consider the projected effective force in the direction of self-propulsion of the tagged particle, which leads to the expression

$$\mathbf{e}\cdot\mathbf{F} = -\bar{\rho}\psi_1\zeta, \quad (21)$$

where ζ is a scalar coefficient that reads

$$\zeta = -\int_0^\infty dr\, r u'(r) \int_0^{2\pi} d\theta \cos\theta \int_0^{2\pi} d\varphi \mathcal{G}(r, \theta, \varphi, t). \quad (22)$$

Similarly, the torque can be expressed as

$$T = -\bar{\rho}\psi_1\varepsilon, \quad (23)$$

where the ε coefficient reads

$$\varepsilon = -\int_0^\infty dr\, r v(r) \int_0^{2\pi} d\theta \int_0^{2\pi} d\varphi w'(\varphi)\mathcal{G}(r, \theta, \varphi, t). \quad (24)$$

We have thus recast the dependence on pair-wise correlations in the two coefficients ζ and ε (see Appendix D 1 for more details).

We now write the force $\mathbf{F}(\mathbf{r}_1, \varphi_1; t)$ in the vector basis defined by the direction of self-propulsion, $\mathbf{e}$, and the gradient of the probability density, $\nabla\psi_1$, following a Gram-Schmidt procedure (see Appendix D 2 for the full derivation), leading to

$$\mathbf{F} \approx (\mathbf{e}\cdot\mathbf{F})\mathbf{e} + (1 - \mathcal{D})\nabla\psi_1, \quad (25)$$

where

$$\mathcal{D} = 1 - \mathbf{F}\cdot[\nabla\psi_1 - (\mathbf{e}\cdot\nabla\psi_1)\mathbf{e}]\frac{1}{|\nabla\psi_1|^2}. \quad (26)$$

This is an approximation as the basis vectors chosen are time dependent and might eventually, although unlikely, become collinear at some particular time during the evolution.

One can then rewrite the one-body Smoluchowski equation, Eq. (17), inserting the projected force, Eq. (21), as well as the expression of the torque, Eq. (23), to obtain

$$\partial_t\psi_1 = -\nabla\cdot[v_{\bar{\rho}}\,\mathbf{e}\psi_1 - \mathcal{D}\nabla\psi_1] + \frac{\partial}{\partial\varphi}\left[\bar{\rho}\psi_1\varepsilon + D_r\frac{\partial\psi_1}{\partial\varphi}\right]. \quad (27)$$

The first term in the right-hand side (RHS) stands for translational advection, defining an effective self-propulsion speed

$$v_{\bar{\rho}} = v_0 - \bar{\rho}\zeta \quad (28)$$

that decays with the mean density $\bar{\rho}$ at a rate given by ζ, which can thus be interpreted as a *translational friction coefficient*, accounting for the arrest of particles in crowded environments and stemming from excluded volume interactions [see Eq. (22)]. The second term in the RHS of Eq. (27) corresponds to translational diffusion with an effective diffusivity $\mathcal{D}$. Following Refs. [30,32], we make the assumption that $\mathcal{D}$ is uniform, corresponding to the long time diffusion coefficient of the system in the passive limit. Such approximation of the effective diffusivity Eq. (26) has been justified and put into test in previous works [32,80]. The diffusivity from the long-time mean-squared displacement can be written as $D = \mathcal{D} + v^2(\rho)/2$, such that in the absence of self-propulsion $\mathcal{D}$ corresponds to the diffusion coefficient of a passive system. This implies that, from now on, all the dependency on pair-wise correlations will be fully encoded in ζ and ε. The effect of the third term in the RHS of Eq. (27) is to advect the orientations. Similar to ζ, ε can be interpreted as a *rotational friction coefficient*. The last term accounts for rotational diffusion.

To proceed, we close the hierarchy of coupled equations by considering the effective friction coefficients as constants [30]. This is the central approximation of our approach which allows us to construct an effective hydrodynamic description. We define the first three moments of the one-body probability distribution, ψ_1, namely, the density field

$$\rho(\mathbf{r}, t) \equiv \int_0^{2\pi} d\varphi\psi_1(\mathbf{r}, \varphi, t), \quad (29)$$

the polarization

$$\mathbf{p}(\mathbf{r}, t) \equiv \int_0^{2\pi} d\varphi\mathbf{e}\psi_1(\mathbf{r}, \varphi, t), \quad (30)$$

and the nematic tensor

$$\mathbf{Q} \equiv \int_0^{2\pi} d\varphi(\mathbf{e}\otimes\mathbf{e} - \mathbb{1}/2)\psi_1(\mathbf{r}, \varphi, t). \quad (31)$$

Integrating the (mean-field) closed evolution equation of the one-body probability distribution, Eq. (27), we obtain the effective hydrodynamic equations for each one of the three fields

$$\partial_t \rho(\mathbf{r},t) = -\boldsymbol{\nabla}\cdot[v_{\bar\rho}\mathbf{p} - \mathcal{D}\boldsymbol{\nabla}\rho], \tag{32}$$

$$\partial_t \mathbf{p}(\mathbf{r},t) = -\boldsymbol{\nabla}\cdot\left[v_{\bar\rho}\left(\tfrac{1}{2}\rho\mathbb{1} + \mathbf{Q}\right) - \mathcal{D}\boldsymbol{\nabla}\mathbf{p}\right] - \bar\rho\varepsilon\mathbf{p}^\perp - D_r\mathbf{p}, \tag{33}$$

$$\partial_t \mathbf{Q}(\mathbf{r},t) = -\boldsymbol{\nabla}\cdot(v_{\bar\rho}\mathbf{Y}) - \tfrac{1}{4}\boldsymbol{\nabla}\otimes(v_{\bar\rho}\mathbf{p}) + \tfrac{1}{4}\boldsymbol{\nabla}^\perp\otimes(v_{\bar\rho}\mathbf{p}^\perp) + \mathcal{D}\nabla^2\mathbf{Q} - 2\bar\rho\varepsilon\mathbf{Q}^\perp - 2D_r\mathbf{Q}, \tag{34}$$

where $\perp$ indicates a rotation corresponding to $\mathbf{p}^\perp = \mathcal{R}\mathbf{p}$, $\boldsymbol{\nabla}^\perp = \mathcal{R}\boldsymbol{\nabla}$, and $\mathbf{Q}^\perp = \mathcal{R}\mathbf{Q}$ with $\mathcal{R} = \left(\begin{smallmatrix}0 & -1\\ 1 & 0\end{smallmatrix}\right)$.

Note that the time evolution equation of each moment is linearly coupled to the next order moment. Consequently, the time evolution of the nematic tensor, Eq. (34), is coupled to the tensor $Y_{\alpha\beta\gamma} \equiv \int_0^{2\pi} d\varphi[e_\alpha e_\beta e_\gamma - \frac{1}{4}(\delta_{\alpha\beta}p_\gamma + \delta_{\alpha\gamma}p_\beta + \delta_{\beta\gamma}p_\alpha)]\psi_1(\mathbf{r},\varphi,t)$, corresponding to the third moment of ψ_1. As it is shown in the next subsection, $\rho(\mathbf{r},t)$ constitutes the slowest moment of the probability distribution. Therefore, higher-order moments are enslaved to $\rho(\mathbf{r},t)$ and become irrelevant for the study of an infinite wavelength instability [40,61]. This remark thus justifies to cut the hierarchy of equations by dropping the dependency on $Y_{\alpha\beta\gamma}$. As a result, we obtain a closed set of hydrodynamic equations accounting for the time evolution of the particle density, polarization vector, and nematic field tensor. Note that the hydrodynamic description we obtained is general and applies to any kind of interaction potentials $\mathcal{U}$ and $\mathcal{H}$. The different behaviors observed for ferromagnetic and nematic alignment have thus to be captured by the coefficients ζ and ε, which contain all the information regarding the microscopic interactions at this level of description.

1. Linear stability analysis

We now assume that the density $\rho(\mathbf{r},t)$ is a slowly varying field. This is justified as long as we are interested in the stability of a homogeneous state. In this case, one can thus replace $\bar\rho$ by the local density field $\rho(\mathbf{r},t)$ in the hydrodynamic equations [30], where now

$$v_{\bar\rho} \;\to\; v[\rho] = v_0 - \rho(\mathbf{r},t)\zeta. \tag{35}$$

We now perform a linear stability analysis of the homogeneous and isotropic solution $(\rho,\mathbf{p},\mathbf{Q}) = (\overline{\rho},0,0)$ of the hydrodynamic equations obtained after such replacement. To this end, we introduce a small perturbation, $\rho(\mathbf{r}) = \bar\rho + \delta\rho$, $\mathbf{p}(\mathbf{r}) = \delta\mathbf{p}$ and $\mathbf{Q}(\mathbf{r}) = \delta\mathbf{Q}$ and obtain a set of five independent linearized equations in Fourier space [see Eqs. (D11) to (D13) in Appendix D 3 for details].

Let us first focus on the linear stability in the absence of alignment interactions. As shown in Ref. [30], considering the density and polarization fields only, the homogeneous solution in this case suffers a long wavelength instability associated to MIPS in a given parameter regime (see Appendix D 4 for full derivation). Adding the nematic field equation does not change this scenario, since Eq. (34) has also a term proportional to the characteristic frequency D_r, ensuring a fast decay. It is then justified to assume that the fast moments, $\hat p_\alpha$ and $\hat Q_{\alpha\beta}$ (where $\hat\ast$ denotes the Fourier transform), are adiabatically enslaved to the slow moment $\hat\rho$, associated to a conserved field (Goldstone theorem).

This also justifies cutting the hierarchy of hydrodynamic equations, Eqs. (32) to (34) on the next (third) order moment $Y_{\alpha\beta\gamma}$, since it also relaxes faster than the density field.

We then perform an adiabatic approximation on the polarization and nematic field, i.e., $\partial_t p_\alpha \approx 0$ and $\partial_t Q_{\alpha\beta} \approx 0$, to obtain an effective diffusion equation in Fourier space,

$$\partial_t \delta\hat\rho(\mathbf{q}) = \mathcal{D}_{\mathbf{q}}^{\rm eff}\mathbf{q}^2\delta\hat\rho(\mathbf{q}), \tag{36}$$

where

$$\mathcal{D}_{\mathbf{q}}^{\rm eff} = \left[\frac{1}{2}(v_0 - \bar\rho\zeta)(v_0 - 2\bar\rho\zeta)\frac{A_{\mathbf{q}}}{A_{\mathbf{q}}^2 + B_{\mathbf{q}}^2} - \mathcal{D}\right], \tag{37}$$

with

$$A_{\mathbf{q}} = -\left\{\left[\frac{1}{4}\frac{(v_0-\bar\rho\zeta)^2}{\mathcal{D}\mathbf{q}^2 + 2D_r}\frac{1}{1+\left(\frac{2\bar\rho\varepsilon}{\mathcal{D}\mathbf{q}^2+2D_r}\right)^2} + \mathcal{D}\right]\mathbf{q}^2 + D_r\right\} \tag{38}$$

$$B_{\mathbf{q}} = -\left[\frac{1}{4}\frac{(v_0-\bar\rho\zeta)^2}{(\mathcal{D}\mathbf{q}^2 + 2D_r)^2}\frac{2\bar\rho\varepsilon}{1+\left(\frac{2\bar\rho\varepsilon}{\mathcal{D}\mathbf{q}^2+2D_r}\right)^2}\mathbf{q}^2 - \bar\rho\varepsilon\right] \tag{39}$$

A linear instability at a wave vector $\mathbf{q}$ is signaled by a negative effective diffusion coefficient $\mathcal{D}_{\mathbf{q}}^{\rm eff} < 0$. The limit of linear stability of the homogenous disordered gas can therefore be computed by setting $\mathcal{D}^{\rm eff} = 0$, which at $\mathbf{q}\to 0$ leads to

$$8\left(\frac{v_0}{v^*} - \tilde\zeta\right)\left(\frac{v_0}{v^*} - 2\tilde\zeta\right)\frac{1}{1+\tilde\varepsilon^2} + 1 = 0. \tag{40}$$

Here, $\frac{v_0}{v^*}$ is the reduced self-propulsion speed, where $v^* = 4\sqrt{\mathcal{D}D_r}$. The translational and rotational friction coefficients are also written in their dimensionless form, $\tilde\zeta = \frac{\bar\rho}{v^*}\zeta$ and $\tilde\varepsilon = \frac{\bar\rho}{D_r}\varepsilon$, and encode all the specificities of the (anisotropic) interactions between particles. Eq. (40) thus constitutes our mean-field prediction of the spinodal of a system of self-propelled disks subjected to generic aligning torques, explicitly written in terms of the relevant nondimensional parameters of the model $(\frac{v_0}{v^*}, \tilde\zeta, \tilde\varepsilon)$.

V. CONTINUUM THEORY VERSUS MICROSCOPIC SIMULATIONS

In this section, we confront quantitatively the prediction from the linear stability of the hydrodynamic equations with direct numerical simulations of ABP with different alignment interactions. To do so, we will employ the Pe as the control parameter quantifying the degree of activity in the system, instead of v_0/v^*, as it is customary in simulations of ABP. Both parameters are related through

$$v_0/v^* = \frac{R}{4\sqrt{\mathcal{D}/D_r}}{\rm Pe} = 0.638{\rm Pe}, \tag{41}$$

where we have numerically computed the value of $\mathcal{D}$, see Appendix E, taken from the long-time diffusion coefficient of a passive system ($v_0 = 0$).

We have derived the evolution equation for the one-body probability distribution ψ_1, where the two-body correlations have been cast into two effective friction coefficients $\tilde{\zeta}$ and $\tilde{\varepsilon}$ which are given by integrals of the the pair correlation function $\mathcal{G}(r,\theta,\varphi,t)$ (we only consider steady states and therefore, from now on, we drop the time dependency). The excluded volume potential imposes a planar rotational symmetry, $\mathcal{G}(r,\theta,\varphi)=\mathcal{G}(r,-\theta,\varphi)$, and the alignment ones (both ferromagnetic and nematic) impose $\mathcal{G}(r,\theta,\varphi)=\mathcal{G}(r,\theta,-\varphi)$. As a result, $\tilde{\varepsilon}=0$ and the limit of stability thus reduces to

$$8\left(\frac{v_0}{v^*}-\tilde{\zeta}\right)\left(\frac{v_0}{v^*}-2\tilde{\zeta}\right)+1=0. \tag{42}$$

To test this prediction against particle-based simulations, we now have to compute $\tilde{\zeta}$ for different values of the microscopic parameters and determine whether they fall or not in the instability region predicted by the hydrodynamic model. As $\tilde{\zeta}$ is given by the pair correlation function, we first start by assessing the impact that the different interactions have on the in-plane structure of the system, defined by coordinates r and θ; see Fig. 5.

To this end, we compute $G(r,\theta)=\int_0^{2\pi}d\varphi\,\mathcal{G}(r,\theta,\varphi)$ using Brownian dynamics simulations. In Fig. 6 we show $G(r,\theta=0)$ and $G(r,\theta=\pi)$, the pair correlation function ahead and behind a tagged particle, for four representative cases: (a) isotropic passive particles, (b) isotropic ABP, (c) ferromagnetic ABP, and (d) nematic ABP; using fixed Pe=16.6 and $g/g_{f,n}=0.4$ (below the onset of orientational order) in the presence of alignment. [In Figs. 12(a)–12(d) in Appendix F we show the full $G(r,\theta)$.] As expected, $G(r,\theta)$ is isotropic for a passive suspension of disks, thus yielding $\zeta=0$. Activity breaks this spatial isotropy: it is more likely for the tagged particle to find other particles in front of it ($\theta=0$) than behind ($\theta=\pi$), giving rise to the self-trapping mechanism at the origin of MIPS. Particles block each other in the direction of self-propulsion, giving rise to a reduction of $v_{\bar{p}}$. Such anisotropy of $G(r,\theta)$ is at the origin of the nonzero value of ζ, which quantifies the decay rate of the self-propulsion speed with the density.

In the presence of ferromagnetic alignment, the structural anisotropy in the system is enhanced as compared to the nonaligning ABP case. The peak structure of $G(r,\theta)$ is more pronounced, as also is the contrast between $G(r,\theta=0)$ and $G(r,\theta=\pi)$. Thus, the mutual kinetic arrest due to collisions just described is also enhanced and as a result also the aggregation of particles. This is in qualitative agreement with our earlier results Fig. 2, showing that MIPS occurs at lower values of Pe and ϕ as the ferromagnetic coupling is increased. The peak structure of $G(r,\theta)$ at short distances in this case also shows that ferromagnetic ABP aggregate into denser structures with a higher degree of spatial order than their isotropic counterpart at a given Pe.

The spatial distribution of particles subjected to nematic alignment seems not to be significantly affected by the presence of torques. In Fig. 6(d) we show $G(r,\theta=\pi)$ and $G(r,\theta=0)$ for a nematic coupling of the same relative strength as the one used for the ferromagnetic case. The results show that nematic alignment does not significantly affect

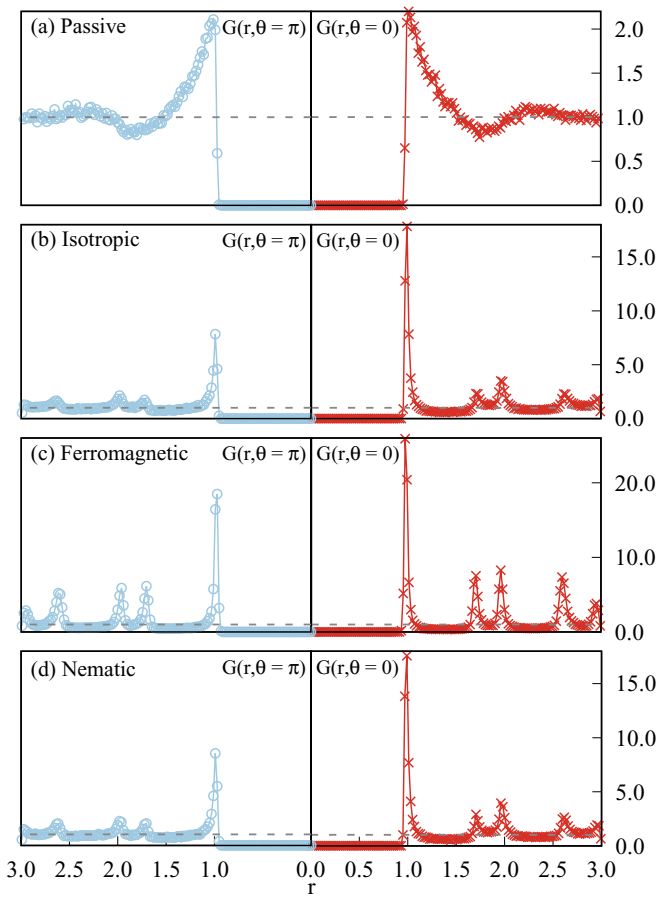

FIG. 6. Radial distribution function along two opposite directions of the (r,θ)-plane, corresponding to the front ($\theta=0$, right column) and the back ($\theta=\pi$, left column) of the tagged particle for (a) Pe $=0$ and $g=0$ (passive suspension); (b) Pe $=16.6$ and $g=0$; (c) Pe $=16.6$ and ferromagnetic $g/g_f=0.4$; (d) Pe $=16.6$ and nematic $g/g_n=0.4$.

the self-trapping phenomenon triggered by the competition between self-propulsion and excluded volume interactions.

Overall, the interpretation of the $G(r,\theta)$ from the viewpoint of the microscopic theory leading to the hydrodynamic equations is in qualitative agreement with the results presented in Figs. 2 and 4. The emergence of MIPS can be understood as particles blocking each other preferentially along their self-propulsion direction, a mechanism well captured by the appearance of anisotropy in the pair correlation functions. Ferromagnetic interactions favor MIPS, while nematic ones do not significantly affect it. In the following, we push this picture further, and show that it can provide a quantitive agreement with particle-based simulations through the calculation of ζ.

The limit of stability of the homogeneous and isotropic phase predicted by the hydrodynamic model in dimensionless units is

$$\tilde{\zeta}^{\pm}=\frac{3}{4}\frac{v_0}{v^*}\pm\frac{1}{4}\sqrt{\left(\frac{v_0}{v^*}\right)^2-1}. \tag{43}$$

In all the region encompassed between $\tilde{\zeta}^-<\tilde{\zeta}<\tilde{\zeta}^+$ the homogeneous state is unstable. This unstable region is repre-

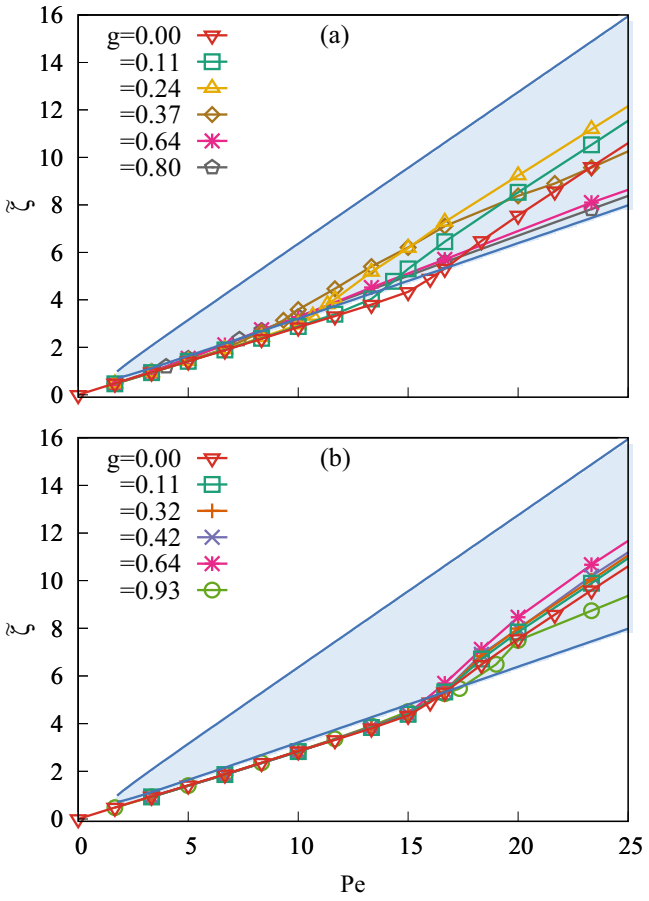

FIG. 7. Linear instability region at $\tilde{\varepsilon} = 0$ (blue region) together with the $\tilde{\zeta}$ coefficient computed from particle-based simulations as a function of the Pe for different values of (a) ferromangetic and (b) nematic alignment strength.

sented in blue in the (Pe, $\tilde{\zeta}$) diagrams, Figs. 7(a) and 7(b). In the same figures we also plot $\tilde{\zeta}$, computed from the $\mathcal{G}(r, \theta, \varphi)$ obtained from Brownian dynamics simulations.

Let us first focus on the numerical values of $\tilde{\zeta}$ computed at $g = 0$ and depicted in Fig. 7 as a function of Pe. As Pe grows, $\tilde{\zeta}$ also does, as a consequence of a larger anisotropy in the pair correlation function for increasing activity. Beyond Pe ≈ 16, the value for which $\tilde{\zeta}$ eventually penetrates the instability region, the rate of growth of $\tilde{\zeta}$ increases significantly. Such behavior is due to the presence of a finite fraction of slow particles belonging to a dense cluster. At large Pe, the slow-down of particles due to the collision persistence is enhanced, triggering the feed-back mechanism by which the phase separation takes place. The value of Pe at which $\tilde{\zeta}$ crosses $\tilde{\zeta}^-$ is identified with the onset of MIPS.

We turn now our attention to the system with ferromagnetic alignment. The values of $\tilde{\zeta}$ extracted from simulations are shown in Fig. 7(a). As we already pointed out, the anisotropy in the correlation function $\mathcal{G}(r, \theta, \varphi)$ is enhanced by the presence of ferromagnetic alignment. As a result, the numerical values of $\tilde{\zeta}$ are now larger than the ones in the $g = 0$ case. The penetration into the instability region happens at lower values of Pe. The values of Pe at which the curves of $\tilde{\zeta}$ enter the instability region are indicated in Fig. 2(a), showing that the prediction of the microscopic theory matches the numerical simulation results accurately.

In the case of nematic alignment, the structural anisotropy of the system is not enhanced as compared to the isotropic $g = 0$ case. Thus, the change in tendency of the numerical values of $\tilde{\zeta}$ and the crossing of the limit of stability happens at approximately the same value of Pe, regardless of the alignment interaction strength; see Fig. 7(b). This prediction also agrees well with the numerical simulation results [Fig. 2(b)].

In our Brownian dynamics simulations, we observed that the region of coexistence is shifted to lower values of Pe as the ferromagnetic coupling is increased [Fig. 4(a)]. On the contrary, for nematic alignment, the coexistence region remains at the same values of Pe within our numerical accuracy; see Fig. 4(b). We can therefore conclude that the results obtained from particle-based simulations and the continuum model are in good agreement, and predict the same phase behavior: ferromagnetic torques enhance the aggregation of particles and the formation of MIPS, while nematic torques have a neutral effect.

VI. CONCLUSIONS

We have introduced a 2D model of spherical Active Brownian Particles, subjected to both excluded volume and velocity-alignment interactions. Our model decouples the alignment mechanism from steric effects, allowing to disentangle these two and tune the strength of nematic or ferromagnetic alignment with no need of introducing shape anisotropy.

We studied such model system both analytically and numerically. First, to grasp the role played by the self-propulsion and alignment strength, we explored the phase behavior of the system by varying the Pe and coupling strength g by means of Brownian dynamics simulations. We identified the emergence of oriented states featuring different collectively moving structures, such as polar and nematic lanes. Unlike systems of self-propelled elongated particles, here the nematic phase keeps the symmetry of the interaction, with no signature of large-scale polar lanes.

We then focused on the main aspect of the present work, namely, phase separation, or MIPS, triggered by the competition between excluded volume effects and self-propulsion in the presence of velocity alignment, yet in the absence of global orientational order. We systematically derived a continuum description of the system taking as a starting point the N-body Smoluchowski equation. This yields a set of coupled hydrodynamic equations for the density, polarization and nematic fields, which directly follow from the microscopic Langevin equations. A key advantage of this approach, which generalizes the work in Ref. [30] to include alignment interactions, is that the resulting field equations are written in terms of the microscopic parameters of the particle-based model, allowing for an explicit comparison between the two, as opposed to more phenomenological approaches based on symmetry arguments [37,77].

The microscopic mechanism giving rise to MIPS within the theory, is a long-wavelength linear instability of the homogenous disordered state due to the anisotropy of the pair distribution function. The latter arises from the fact that

particles have a higher tendency to collide with their neighbors along the direction of self-propulsion, leading to the formation of clusters and eventually a full phase separation. We have shown that such self-trapping mechanism is enhanced in the presence of ferromagnetic alignment but remains largely unaffected in the nematic case. The predictions of the onset of MIPS from the microscopic theory agree quantitatively with particle-based simulations.

We showed that the mechanism behind MIPS appears to be preserved in the presence of alignment interactions. The present study opens the possibility of extending the this formalism to study more complex situations. For instance, studying how chirality (circle swimming) [81–84], quench disorder [85–87] or other kind of interactions [88–90] affect MIPS, constitute interesting lines of future investigation. Here, we have focused on the long-wavelength instability of the disordered state. However, other linear instabilities can take place. This means that, in different parameter regimes, the theory might be able to account for the richness of different structures observed in particle-based simulations across the phase diagram. As a next step, it would be very interesting to extend the theory and explore all the unstable modes associated to both the homogeneous disordered state and the homogeneous oriented one. We leave this challenging task for future work.

ACKNOWLEDGMENTS

E.S.-S. thanks Joan Codina for helpful discussions. D.L. acknowledges Ministerio de Ciencia, Innovación y Universidades MCIU/AEI/FEDER for financial support under Grant Agreement No. RTI2018-099032-J-I00. I.P. acknowledges support from Ministerio de Ciencia, Innovación y Universidades MCIU/AEI/FEDER for financial support under Grant Agreement No. PGC2018-098373-B-100 AEI/FEDER-EU and from Generalitat de Catalunya under Project No. 2017SGR-884. E.S.-S. and I.P. acknowledge Swiss National Science Foundation Project No. 200021-175719.

APPENDIX A: DERIVATION OF THE NEMATIC TORQUE

We write the Hamiltonian of a system of N particles subjected to a local nematic alignment interaction,

$$\mathcal{H} = -J \sum_i \sum_{j\in\omega_i} \mathbf{q}_i \cdot \mathbf{q}_j, \tag{A1}$$

where the uniaxial nematic tensor reads $\mathbf{q}_i = \mathbf{e}_i \otimes \mathbf{e}_i - \frac{1}{2}\mathbb{1}$ and $\mathbf{e}_i = (\cos\varphi_i, \sin\varphi_i)$ and $\mathbf{a}\cdot\mathbf{b} = \mathrm{Tr}(\mathbf{ab})$. In the case of study, the trace can be expressed as

$$\mathrm{Tr}(\mathbf{q}_i\mathbf{q}_j) = \tfrac{1}{2}(\cos 2\varphi_i \cos 2\varphi_j + \sin 2\varphi_i \sin 2\varphi_j). \tag{A2}$$

Using the trigonometric relation $\cos(\varphi_i - \varphi_j) = \cos\varphi_i\cos\varphi_j + \sin\varphi_i\sin\varphi_j$, it is possible to rewrite the Hamiltonian in terms of the phase difference $\varphi_{ij} = \varphi_i - \varphi_j$,

$$\mathcal{H} = -J \sum_i \sum_{j\in\omega_i} \frac{1}{2}\cos(2\varphi_{ij}). \tag{A3}$$

Further trigonometric relations can be used to write the Hamiltonian in different ways, such as $\cos(2\varphi_{ij}) = 2\cos^2(\varphi_{ij}) - 1$, which leads to

$$\mathcal{H} = -J \sum_i \sum_{j\in\omega_i} \left(\cos^2\varphi_{ij} - \frac{1}{2}\right). \tag{A4}$$

Deriving with respect to an angle on gets the desired expression for the torque,

$$T_i = -\frac{\partial\mathcal{H}}{\partial\varphi_i} = -J\sum_j \sin(2\varphi_{ij}). \tag{A5}$$

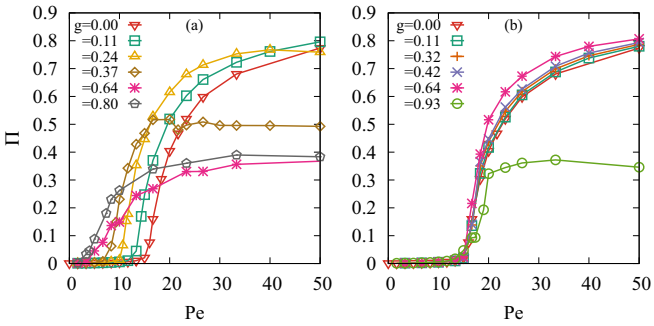

FIG. 8. Probability to belong to the largest cluster as a function of the normalized swimming speed Pe at different values of the (a) ferromagnetic and (b) nematic alignment strengths.

APPENDIX B: CHARACTERIZATION OF MIPS

We compute the fraction of particles in the largest cluster of the system, Π (Fig. 8). Clusters are defined by setting a threshold distance below which two particles are considered to belong to the same cluster. Here, we set this threshold to be the cutoff distance of the steric potential, $R = 1$, and we compute Π as a function of Pe. As Pe increases, collisions between self-propelled particles become more probable, thus enhancing mutual blocking due to the swimming persistence. This leads to further aggregation between particles and, consequently, to the growth of Π.

Nevertheless, the curves of Π(Pe) do not tend to $\Pi = 1$ as Pe is increased, but they saturate at lower values of Π, when g approaches the flocking phase transition from below. This is due to the fact that local orientational correlations grow at $g \neq 0$, setting a different characteristic interparticle length than the one induced by purely excluded volume interactions. As a result, particles are further apart and clusters defined according to the cutoff distance $R = 1$ are now smaller in size.

APPENDIX C: FINITE-SIZE EFFECTS

We plot in Fig. 9 the binodals at a fixed nematic alignment strength $g = 0.64$ and for three different system sizes $N = 4000, 8000, 16\,000$.

In the same spirit, we also compute the numerical values of $\tilde{\zeta}$ at fixed nematic alignment strength $g = 0.64$ for system sizes $N = 8000, 16\,000$ (Fig. 10). We observe that the penetration of $\tilde{\zeta}$ into the instability region occurs at the same value of Pe as it does for $N = 4000$, within numerical accuracy.

We can therefore state that the numerical data obtained at $N = 8000, 16\,000$ agree well with the one obtained at

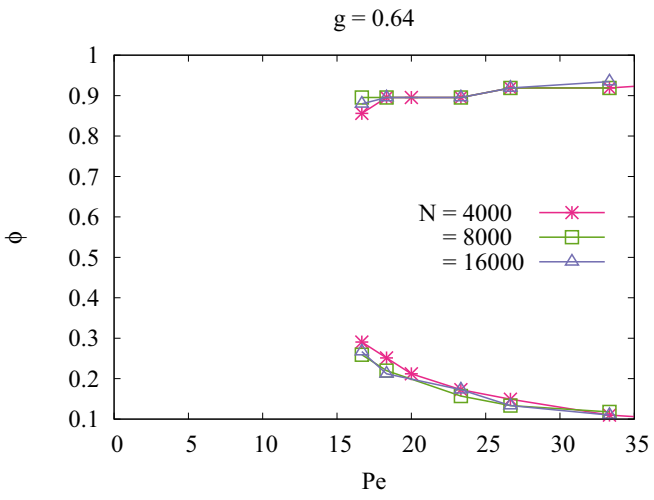

FIG. 9. Phase coexistence regions for fixed nematic alignment strength $g=0.64$ and different system sizes $N=4000$, 8000, 16 000.

$N = 4000$, showing the robustness of the results presented to characterize the phase separation induced by the motility.

APPENDIX D: CONTINUUM MODEL

1. Expressions of force and torque

The mean force and torque exerted by the surrounding particles into the tagged particle (labeled *1*) are expressed as

$$\mathbf{F}(\mathbf{r}_1,\varphi_1;t) = \int_{-\infty}^{\infty} d\mathbf{r}_2 \int_0^{2\pi} d\varphi_2 u'(r_{12}) \frac{\mathbf{r}_{12}}{r_{12}} \psi_2, \tag{D1}$$

and the mean torque is

$$T(\mathbf{r}_1,\varphi_1;t) = \int_{-\infty}^{\infty} d\mathbf{r}_2 \int_0^{2\pi} d\varphi_2 v(r_{12}) w'(\varphi_{12}) \psi_2. \tag{D2}$$

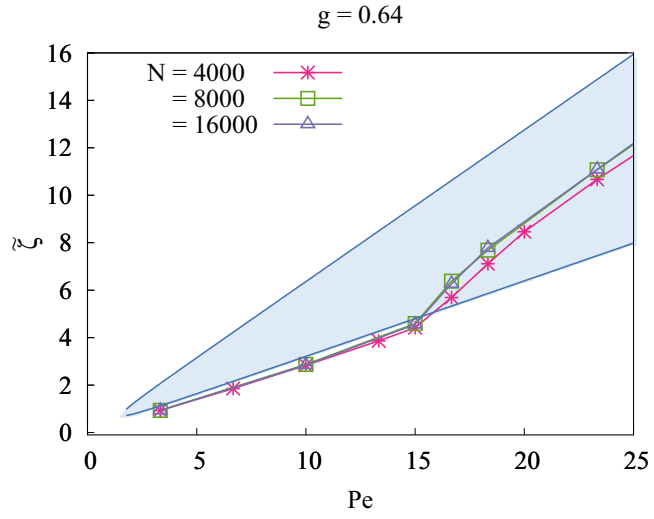

FIG. 10. Linear instability region at $\tilde{\varepsilon} = 0$ (blue region) together with the $\tilde{\zeta}$ coefficient computed from particle-based simulations as a function of the Pe for a fixed nematic alignment strength $g = 0.64$ and different system sizes $N = 4000$, 8000, 16 000.

Introducing the decomposition of $\psi_2(\mathbf{r}_1,\mathbf{r}_2,\varphi_1,\varphi_2,t)$ stated in Eq. (20), as well as the changes of variables $\mathbf{r}_{12} = \mathbf{r}_2 - \mathbf{r}_1$ and $\varphi_{12} = \varphi_2 - \varphi_1$, which yield $d\mathbf{r}_{12} = d\mathbf{r}_2$ and $d\varphi_{12} = d\varphi_2$, it is possible to rewrite Eq. (D2) as

$$\mathbf{F}(\mathbf{r}_1,\varphi_1;t) = \bar{\rho}\psi_1(\mathbf{r}_1,\varphi_1,t) \int_{-\infty}^{\infty} d\mathbf{r}_{12} \int_0^{2\pi} d\varphi_{12} \times u'(r_{12}) \frac{\mathbf{r}_{12}}{r_{12}} \mathcal{G}(r_{12},\theta,\varphi_{12},t), \tag{D3}$$

$$T(\mathbf{r}_1,\varphi_1;t) = \bar{\rho}\psi_1(\mathbf{r}_1,\varphi_1,t) \int_{-\infty}^{\infty} d\mathbf{r}_{12} \int_0^{2\pi} d\varphi_{12} \times v(r_{12}) w'(\varphi_{12}) \mathcal{G}(r_{12},\theta,\varphi_{12},t). \tag{D4}$$

It is straightforward to see that the projection of the force in the direction of self-propulsion, $\mathbf{e}$, can be expressed as $\mathbf{e}\cdot\mathbf{F} = -\bar{\rho}\psi_1\zeta$, where ζ has the functional form Eq. (22). Similarly, the torque can also be decomposed in $T = -\bar{\rho}\psi_1\varepsilon$, where ε is expressed as in Eq. (24).

2. Gram-Schmidt orthonormalization of the force

We perform a Gram-Schmidt orthonormalization on the force $\mathbf{F}$ to decompose it in the vector basis formed by the direction of self-propulsion and the gradient of the probability distribution, $\{\mathbf{e}, \nabla\psi_1\}$.

We pick the first vector of the orthonormal set $\{\mathbf{u}_1, \mathbf{u}_2\}$ we want to construct, $\mathbf{u}_1 = \mathbf{e}$. This one already fulfils $|\mathbf{e}| = 1$. Then the second vector is

$$\mathbf{u}_2 = \nabla_1\psi_1 - \mathrm{proj}_{\mathbf{u}_1}(\nabla_1\psi_1), \tag{D5}$$

where the projection operator is $\mathrm{proj}_{\mathbf{a}}(\mathbf{b}) = \frac{\mathbf{a}\cdot\mathbf{b}}{\mathbf{a}\cdot\mathbf{a}}\mathbf{a}$, giving the projection of vector $\mathbf{b}$ along the axis spanned by $\mathbf{a}$. Thus, we can rewrite Eq. (D5),

$$\mathbf{u}_2 = \nabla_1\psi_1 - (\mathbf{e}\cdot\nabla_1\psi_1)\mathbf{e}. \tag{D6}$$

We now proceed to normalize $\mathbf{u}_2$,

$$\mathbf{u}_2 = \frac{\nabla_1\psi_1 - (\mathbf{e}\cdot\nabla_1\psi_1)\mathbf{e}}{|\nabla_1\psi_1 - (\mathbf{e}\cdot\nabla_1\psi_1)\mathbf{e}|}. \tag{D7}$$

We have thus constructed an orthonormal vector basis. We can now decompose the force,

$$\begin{aligned}\mathbf{F} &= (\mathbf{e}\cdot\mathbf{F})\mathbf{e} \\ &\quad + \left(\frac{\nabla_1\psi_1 - (\mathbf{e}\cdot\nabla_1\psi_1)\mathbf{e}}{|\nabla_1\psi_1 - (\mathbf{e}\cdot\nabla_1\psi_1)\mathbf{e}|}\cdot\mathbf{F}\right)\frac{\nabla_1\psi_1 - (\mathbf{e}\cdot\nabla_1\psi_1)\mathbf{e}}{|\nabla_1\psi_1 - (\mathbf{e}\cdot\nabla_1\psi_1)\mathbf{e}|} \\ &= \left[(\mathbf{e}\cdot\mathbf{F}) - \left(\frac{(\nabla_1\psi_1 - (\mathbf{e}\cdot\nabla_1\psi_1)\mathbf{e})\cdot\mathbf{F}}{|\nabla_1\psi_1 - (\mathbf{e}\cdot\nabla_1\psi_1)\mathbf{e}|^2}\right)(\mathbf{e}\cdot\nabla_1\psi_1)\right]\mathbf{e} \\ &\quad + \left(\frac{(\nabla_1\psi_1 - (\mathbf{e}\cdot\nabla_1\psi_1)\mathbf{e})\cdot\mathbf{F}}{|\nabla_1\psi_1 - (\mathbf{e}\cdot\nabla_1\psi_1)\mathbf{e}|^2}\right)\nabla_1\psi_1.\end{aligned} \tag{D8}$$

We first consider that the projection of the force along $\frac{\nabla_1\psi_1 - (\mathbf{e}\cdot\nabla_1\psi_1)\mathbf{e}}{|\nabla_1\psi_1 - (\mathbf{e}\cdot\nabla_1\psi_1)\mathbf{e}|}$ is much smaller than its projection along $\mathbf{e}$. Second, we also consider that $|\nabla_1\psi_1 - (\mathbf{e}\cdot\nabla_1\psi_1)\mathbf{e}|^2 \approx |\nabla_1\psi_1|^2$, assuming that $\mathbf{e}$ and $\nabla_1\psi_1$ are "almost"

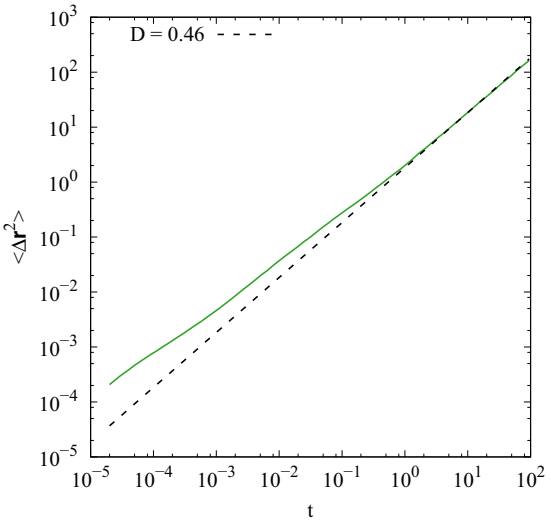

FIG. 11. Log-log plot of the mean-squared displacement for a passive system of particles at packing fraction $\phi = 0.4$.

perpendicular vectors. This leads to

$$\mathbf{F} \approx (\mathbf{e}\cdot\mathbf{F})\mathbf{e} + \left(\frac{(\nabla_1\psi_1 - (\mathbf{e}\cdot\nabla_1\psi_1)\mathbf{e})\cdot\mathbf{F}}{|\nabla_1\psi_1|^2}\right)\nabla_1\psi_1$$
$$= (\mathbf{e}\cdot\mathbf{F})\mathbf{e} + (1-\mathcal{D})\nabla\psi_1, \tag{D9}$$

where the first term on the right-hand side corresponds to Eq. (21) and $\mathcal{D}$ corresponds to Eq. (26).

3. Fourier transform of the hydrodynamic equation

Writing Eqs. (32) to (34) in Fourier space,

$$\mathbf{u} \sim \hat{\mathbf{u}} e^{i\mathbf{q}\cdot\mathbf{r}}, \tag{D10}$$

where $\mathbf{u} = (\delta\rho, \delta p_x, \delta p_y, \delta Q_{xx}, \delta Q_{xy})$, we obtain the following time evolution equations for the perturbation,

$$\partial_t \delta\hat{\rho} = -iq_\beta[(v_0 - \bar{\rho}\zeta)\delta\hat{p}_\beta - iq_\beta\mathcal{D}\delta\hat{\rho}], \tag{D11}$$

$$\partial_t \delta\hat{p}_\alpha = -iq_\beta\big[\tfrac{1}{2}(v_0 - 2\bar{\rho}\zeta)\delta\hat{\rho}\delta_{\alpha\beta} + (v_0 - \bar{\rho}\zeta)\delta\hat{Q}_{\alpha\beta} - iq_\beta\mathcal{D}\delta\hat{p}_\alpha\big] - \bar{\rho}\varepsilon\delta\hat{p}^{\perp}_\alpha - D_r\delta\hat{p}_\alpha, \tag{D12}$$

$$\partial_t \delta\hat{Q}_{\alpha\beta} = -iq_\gamma\big[(v_0 - \bar{\rho}\zeta)\big(-\tfrac{1}{2}\delta_{\alpha\beta}\delta\hat{p}_\gamma + \tfrac{1}{4}(\delta_{\alpha\beta}\delta\hat{p}_\gamma + \delta_{\alpha\gamma}\delta\hat{p}_\beta + \delta_{\beta\gamma}\delta\hat{p}_\alpha)\big) - iq_\gamma\mathcal{D}\delta\hat{Q}_{\alpha\beta}\big] - 2\bar{\rho}\varepsilon\delta\hat{Q}^{\perp}_{\alpha\beta} - 2D_r\delta\hat{Q}_{\alpha\beta}, \tag{D13}$$

where q_β is the β-component of the wave vector. Equations (D11) to (D13)) constitute a system of five independent evolution equations (the nematic tensor has just two independent components due to the traceless and symmetric conditions).

4. Linear stability analysis of a system of isotropic repulsive disks

We consider a system of isotropic polar active disks without alignment interactions. Since there are no local torques ($\varepsilon = 0$) and the only effective interaction between particles is of steric origin, we cut the hierarchy of effective hydrodynamic equations to first order. Hence, the time evolution

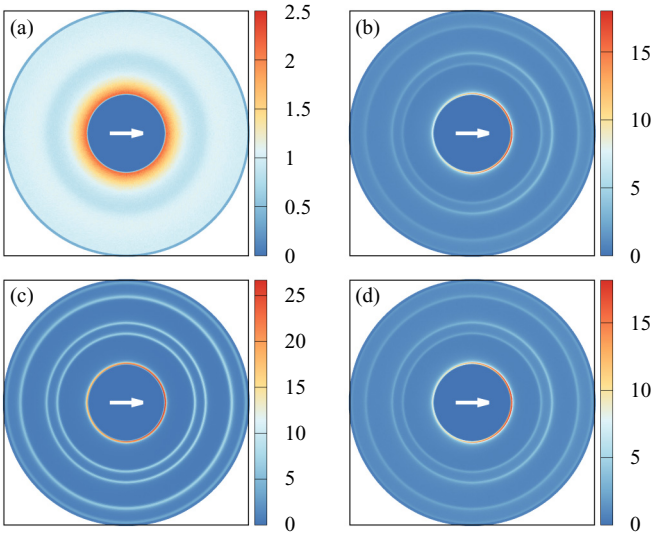

FIG. 12. Correlation function $G(r,\theta)$ of a particle in a system at $\phi = 0.4$ for parameters (a) Pe $= 0$ and $g = 0$ (passive suspension); (b) Pe $= 16.6$ and $g = 0$; (c) Pe $= 16.6$ and ferromagnetic $g/g_f = 0.4$; (d) Pe $= 16.6$ and nematic $g/g_n = 0.4$. The front of the particle is marked by the white arrow, corresponding to $\theta = 0$.

for the density and the polarization field in Fourier space now reads

$$\partial_t \delta\hat{\rho} = -iq_\beta[(v_0 - \bar{\rho}\zeta)\delta\hat{p}_\beta - iq_\beta\mathcal{D}\delta\hat{\rho}], \tag{D14}$$

$$\partial_t \delta\hat{p}_\alpha = -iq_\beta\big[\tfrac{1}{2}(v_0 - 2\bar{\rho}\zeta)\delta\hat{\rho}\delta_{\alpha\beta} - iq_\beta\mathcal{D}\delta\hat{p}_\alpha\big] - D_r\delta\hat{p}_\alpha. \tag{D15}$$

Writing the system of equations in matrix form $\partial_t(\delta\hat{\rho}\ \delta\hat{p}_x\ \delta\hat{p}_y)^T = M(\delta\hat{\rho}\ \delta\hat{p}_x\ \delta\hat{p}_y)^T$, where

$$M = \begin{bmatrix} -\mathcal{D}\mathbf{q}^2 & -i(v_0 - \bar{\rho}\zeta)q_x & -i(v_0 - \bar{\rho}\zeta)q_y \\ -i\frac{1}{2}(v_0 - 2\bar{\rho}\zeta)q_x & -(\mathcal{D}\mathbf{q}^2 + D_r) & 0 \\ -i\frac{1}{2}(v_0 - 2\bar{\rho}\zeta)q_y & 0 & -(\mathcal{D}\mathbf{q}^2 + D_r) \end{bmatrix},$$

it is possible to compute its eigenvalues $\det(M - \lambda\mathbb{1}) = 0$, which are

$$\lambda_1 = -(D_r + \mathcal{D}\mathbf{q}^2),$$
$$\lambda_2 = -\tfrac{1}{2}(2\mathcal{D}\mathbf{q}^2 + D_r) + \tfrac{1}{2}\sqrt{D_r^2 - 2\mathbf{q}^2(v_0 - \bar{\rho}\zeta)(v_0 - 2\bar{\rho}\zeta)},$$
$$\lambda_3 = -\tfrac{1}{2}(2\mathcal{D}\mathbf{q}^2 + D_r) - \tfrac{1}{2}\sqrt{D_r^2 - 2\mathbf{q}^2(v_0 - \bar{\rho}\zeta)(v_0 - 2\bar{\rho}\zeta)}. \tag{D16}$$

We subsequently expand the eigenvalues up to second order,

$$\lambda_1 = -(\mathcal{D}\mathbf{q}^2 + D_r),$$
$$\lambda_2 = -1 + \left[-\mathcal{D} + \frac{(v_0 - \bar{\rho}\zeta)(v_0 - 2\bar{\rho}\zeta)}{2D_r}\right]\mathbf{q}^2 + \mathcal{O}(\mathbf{q}^3),$$
$$\lambda_3 = 0 + \left[-\mathcal{D} - \frac{(v_0 - \bar{\rho}\zeta)(v_0 - 2\bar{\rho}\zeta)}{2D_r}\right]\mathbf{q}^2 + \mathcal{O}(\mathbf{q}^3). \tag{D17}$$

Out of the three eigenvalues, the only mode which can become unstable (positive) is λ_3. The limit of stability is given by

$$\zeta = \frac{3}{4}\frac{v_0}{\bar{\rho}} \pm \frac{1}{4\bar{\rho}}\sqrt{v_0^2 - 16\mathcal{D}D_r}. \tag{D18}$$

APPENDIX E: COMPUTATION OF PARAMETERS

We compute the long-time diffusion coefficient, $\mathcal{D}$, which will allow us to calculate numerically the normalization factor of the self-propulsion speed, $v^* = 4\sqrt{\mathcal{D}D_r}$. To this end, we measure the mean-squared angular displacement of a passive system of particles at $\phi = 0.4$, $\mathcal{D} = \lim_{t\to\infty} \frac{1}{4t}\langle[\mathbf{r}(t) - \mathbf{r}(0)]^2\rangle$. The value of the fit corresponds to $\mathcal{D} = 0.46$, Fig. 11, which is in good agreement with previous results in the literature [30].

APPENDIX F: CORRELATION FUNCTION IN THE (r, θ)-PLANE

In the absence of both self-propulsion and local alignment, the correlation function $G(r, \theta)$ is spatially isotropic, as depicted in Fig. 12. It is thus equally probable to find a particle in front than behind the tagged particle, represented by a white arrow. Introducing a finite self-propulsion speed breaks the spatial isotropy, making it more probable to find particles in front than behind the tagged particle [Fig. 12(b)]. Ferromagnetic alignment further enhances the spatial structure in the plane and the anisotropy between the front and the back of particles [Fig. 12(c)]. On the contrary, nematic alignment leaves the spatial structure unchanged [Fig. 12(d)], with respect to the case with no alignment.

[1] C. Bechinger, R. Di Leonardo, H. Löwen, C. Reichhardt, G. Volpe, and G. Volpe, Active particles in complex and crowded environments, Rev. Mod. Phys. **88**, 045006 (2016).

[2] W. Bialek, A. Cavagna, I. Giardina, T. Mora, E. Silvestri, M. Viale, and A. M. Walczak, Statistical mechanics for natural flocks of birds, Proc. Natl. Acad. Sci. USA **109**, 4786 (2012).

[3] A. Sokolov, I. S. Aranson, J. O. Kessler, and R. E. Goldstein, Concentration Dependence of the Collective Dynamics of Swimming Bacteria, Phys. Rev. Lett. **98**, 158102 (2007).

[4] H. P. Zhang, A. Be'er, E. L. Florin, and H. L. Swinney, Collective motion and density fluctuations in bacterial colonies, Proc. Natl. Acad. Sci. USA **107**, 13626 (2010).

[5] D. Nishiguchi, K. H. Nagai, H. Chaté, and M. Sano, Long-range nematic order and anomalous fluctuations in suspensions of swimming filamentous bacteria, Phys. Rev. E **95**, 020601(R) (2017).

[6] A. Be'er and G. Ariel, A statistical physics view of swarming bacteria, Mov. Ecol. **7**, 9 (2019).

[7] J. O. Kessler, Individual and collective fluid dynamics of swimming cells, J. Fluid Mech. **173**, 191 (1986).

[8] T. B. Saw, A. Doostmohammadi, V. Nier, L. Kocgozlu, S. Thampi, Y. Toyama, P. Marcq, C. T. Lim, J. M. Yeomans, and B. Ladoux, Topological defects in epithelia govern cell death and extrusion, Nature (London) **544**, 212 (2017).

[9] C. Malinverno, S. Corallino, F. Giavazzi, M. Bergert, Q. Li, M. Leoni, A. Disanza, E. Frittoli, A. Oldani, E. Martini *et al.*, Endocytic reawakening of motility in jammed epithelia, Nat. Mater. **16**, 587 (2017).

[10] V. Schaller, C. Weber, C. Semmrich, E. Frey, and A. R. Bausch, Polar patterns of driven filaments, Nature (London) **467**, 73 (2010).

[11] Y. Sumino, K. H. Nagai, Y. Shitaka, D. Tanaka, K. Yoshikawa, H. Chaté, and K. Oiwa, Large-scale vortex lattice emerging from collectively moving microtubules, Nature (London) **483**, 448 (2012).

[12] D. Inoue, B. Mahmot, A. M. R. Kabir, T. I. Farhana, K. Tokuraku, K. Sada, A. Konagaya, and A. Kakugo, Depletion force induced collective motion of microtubules driven by kinesin, Nanoscale **7**, 18054 (2015).

[13] D. Needleman and Z. Dogic, Active matter at the interface between materials science and cell biology, Nat. Rev. Mater. **2**, 17048 (2017).

[14] I. Buttinoni, J. Bialké, F. Kümmel, H. Löwen, C. Bechinger, and T. Speck, Dynamical Clustering and Phase Separation in Suspensions of Self-Propelled Colloidal Particles, Phys. Rev. Lett. **110**, 238301 (2013).

[15] A. Bricard, J.-B. Caussin, N. Desreumaux, O. Dauchot, and D. Bartolo, Emergence of macroscopic directed motion in populations of motile colloids, Nature (London) **503**, 95 (2013).

[16] F. Ginot, I. Theurkauff, D. Levis, C. Ybert, L. Bocquet, L. Berthier, and C. Cottin-Bizonne, Nonequilibrium Equation of State in Suspensions of Active Colloids, Phys. Rev. X **5**, 011004 (2015).

[17] J. Deseigne, O. Dauchot, and H. Chaté, Collective Motion of Vibrated Polar Disks, Phys. Rev. Lett. **105**, 098001 (2010).

[18] V. Narayan, S. Ramaswamy, and N. Menon, Long-lived giant number fluctuations in a swarming granular nematic, Science **317**, 105 (2007).

[19] C. Scholz, M. Engel, and T. Pöschel, Rotating robots move collectively and self-organize, Nat. Phys. Commun. **9**, 931 (2018).

[20] I. Theurkauff, C. Cottin-Bizonne, J. Palacci, C. Ybert, and L. Bocquet, Dynamic Clustering in Active Colloidal Suspensions with Chemical Signaling, Phys. Rev. Lett. **108**, 268303 (2012).

[21] F. Ginot, I. Theurkauff, F. Detcheverry, C. Ybert, and C. Cottin-Bizonne, Aggregation-fragmentation and individual dynamics of active clusters, Nat. Commun. **9**, 696 (2018).

[22] D. Geyer, D. Martin, J. Tailleur, and D. Bartolo, Freezing a Flock: Motility-Induced Phase Separation in Polar Active Liquids, Phys. Rev. X **9**, 031043 (2019).

[23] M. C. Marchetti, J.-F. Joanny, S. Ramaswamy, T. B. Liverpool, J. Prost, M. Rao, and R. A. Simha, Hydrodynamics of soft active matter, Rev. Mod. Phys **85**, 1143 (2013).

[24] M. R. Shaebani, A. Wysocki, R. G. Winkler, G. Gompper, and H. Rieger, Computational models for active matter, Nat. Rev. Phys. **2**, 181 (2020).

[25] H. Chaté, Dry aligning dilute active matter, Annu. Rev. Condens. Matter Phys. **11**, 189 (2020).

[26] M. F. Hagan and A. Baskaran, Emergent self-organization in active materials, Curr. Opin. Cell Biol. **38**, 74 (2016).

[27] U. Erdmann, W. Ebeling, L. Schimansky-Geier, and F. Schweitzer, Brownian particles far from equilibrium, Eur. Phys. J. B **15**, 105 (2000).

[28] B. ten Hagen, S. van Teeffelen, and H. Löwen, Brownian motion of a self-propelled particle, J. Phys.: Condens. Matter **23**, 194119 (2011).

[29] P. Romanczuk, M. Bär, W. Ebeling, B. Lindner, and L. Schimansky-Geier, Active Brownian particles: From individual to collective stochastic dynamics: From individual to collective stochastic dynamics, Eur. Phys. J. Spec. Top. **202**, 1 (2012).

[30] J. Bialké, H. Löwen, and T. Speck, Microscopic theory for the phase separation of self-propelled repulsive disks, Europhys. Lett. **103**, 30008 (2013).

[31] T. Speck, J. Bialké, A. M. Menzel, and H. Löwen, Effective Cahn-Hilliard Equation for the Phase Separation of Active Brownian Particles, Phys. Rev. Lett. **112**, 218304 (2014).

[32] T. Speck, A. M. Menzel, J. Bialké, and H. Löwen, Dynamical mean-field theory and weakly nonlinear analysis for the phase separation of active Brownian particles, J. Chem. Phys. **142** (2015).

[33] R. Wittkowski, A. Tiribocchi, J. Stenhammar, R. J. Allen, D. Marenduzzo, and M. E. Cates, Scalar φ 4 field theory for active-particle phase separation, Nat. Commun. **5**, 4351 (2014).

[34] C. Nardini, É. Fodor, E. Tjhung, F. van Wijland, J. Tailleur, and M. E. Cates, Entropy Production in Field Theories Without Time-Reversal Symmetry: Quantifying the Nonequilibrium Character of Active Matter, Phys. Rev. X **7**, 021007 (2017).

[35] M. Paoluzzi, C. Maggi, and A. Crisanti, Statistical field theory and effective action method for scalar active matter, Phys. Rev. Research **2**, 023207 (2020).

[36] J. Bickmann and R. Wittkowski, Predictive local field theory for interacting active Brownian spheres in two spatial dimensions, J. Phys.: Condens. Matter **32**, 214001 (2020).

[37] M. E. Cates, Active field theories, arXiv:1904.01330 (2019).

[38] M. E. Cates and J. Tailleur, Motility-induced phase separation, Annu. Rev. Condens. Matter Phys. **6**, 219 (2015).

[39] J. Tailleur and M. E. Cates, Statistical Mechanics of Interacting Run-and-Tumble Bacteria, Phys. Rev. Lett. **100**, 218103 (2008).

[40] M. E. Cates and J. Tailleur, When are active Brownian particles and run-and-tumble particles equivalent? consequences for motility-induced phase separation, Europhys. Lett. **101**, 20010 (2013).

[41] Y. Fily and M. C. Marchetti, Athermal Phase Separation of Self-Propelled Particles with no Alignment, Phys. Rev. Lett. **108**, 235702 (2012).

[42] G. S. Redner, M. F. Hagan, and A. Baskaran, Structure and Dynamics of a Phase-Separating Active Colloidal Fluid, Phys. Rev. Lett. **110**, 055701 (2013).

[43] J. Stenhammar, D. Marenduzzo, R. J. Allen, and M. E. Cates, Phase behaviour of active Brownian particles: The role of dimensionality, Soft Matter **10**, 1489 (2014).

[44] A. Wysocki, R. G. Winkler, and G. Gompper, Cooperative motion of active Brownian spheres in three-dimensional dense suspensions, Europhys. Lett. **105**, 48004 (2014).

[45] D. Levis, J. Codina, and I. Pagonabarraga, Active Brownian equation of state: Metastability and phase coexistence, Soft Matter **13**, 8113 (2017).

[46] A. P. Solon, J. Stenhammar, M. E. Cates, Y. Kafri, and J. Tailleur, Generalized thermodynamics of phase equilibria in scalar active matter, Phys. Rev. E **97**, 020602(R) (2018).

[47] P. Digregorio, D. Levis, A. Suma, L. F. Cugliandolo, G. Gonnella, and I. Pagonabarraga, Full Phase Diagram of Active Brownian Disks: From Melting to Motility-Induced Phase Separation, Phys. Rev. Lett. **121**, 098003 (2018).

[48] C. B. Caporusso, P. Digregorio, D. Levis, L. F. Cugliandolo, and G. Gonnella, Motility-Induced Microphase and Macrophase Separation in a Two-Dimensional Active Brownian Particle System, Phys. Rev. Lett. **125**, 178004 (2020).

[49] B. Partridge and C. F. Lee, Critical Motility-Induced Phase Separation Belongs to the Ising Universality Class, Phys. Rev. Lett. **123**, 068002 (2019).

[50] T. Vicsek, A. Czirók, E. Ben-Jacob, I. Cohen, and O. Shochet, Novel Type of Phase Transition in a System of Self-Driven Particles, Phys. Rev. Lett. **75**, 1226 (1995).

[51] J. Toner and Y. Tu, Long-Range Order in a Two-Dimensional Dynamical *XY* Model: How Birds Fly Together, Phys. Rev. Lett. **75**, 4326 (1995).

[52] F. Ginelli, F. Peruani, M. Bär, and H. Chaté, Large-Scale Collective Properties of Self-Propelled Rods, Phys. Rev. Lett. **104**, 184502 (2010).

[53] A. Peshkov, I. S. Aranson, E. Bertin, H. Chaté, and F. Ginelli, Nonlinear Field Equations for Aligning Self-Propelled Rods, Phys. Rev. Lett. **109**, 268701 (2012).

[54] E. Bertin, A. Baskaran, H. Chaté, and M. C. Marchetti, Comparison between Smoluchowski and Boltzmann approaches for self-propelled rods, Phys. Rev. E **92**, 042141 (2015).

[55] B. Mahault and H. Chaté, Long-Range Nematic Order in Two-Dimensional Active Matter, Phys. Rev. Lett. **127**, 048003 (2021).

[56] M. Bär, R. Großmann, S. Heidenreich, and F. Peruani, Self-propelled rods: Insights and perspectives for active matter, Annu. Rev. Condens. Matter Phys. **11**, 441 (2020).

[57] F. Peruani, A. Deutsch, and M. Bär, Nonequilibrium clustering of self-propelled rods, Phys. Rev. E **74**, 030904(R) (2006).

[58] M. Abkenar, K. Marx, T. Auth, and G. Gompper, Collective behavior of penetrable self-propelled rods in two dimensions, Phys. Rev. E **88**, 062314 (2013).

[59] S. Weitz, A. Deutsch, and F. Peruani, Self-propelled rods exhibit a phase-separated state characterized by the presence of active stresses and the ejection of polar clusters, Phys. Rev. E **92**, 012322 (2015).

[60] X. Q. Shi and H. Chate, Self-propelled rods: Linking alignment-dominated and repulsion-dominated active matter, arXiv:1807.00294v2 (2018).

[61] R. Van Damme, J. Rodenburg, R. Van Roij, and M. Dijkstra, Interparticle torques suppress motility-induced phase separation for rodlike particles, J. Chem. Phys. **150**, 164501 (2019).

[62] A. Jayaram, A. Fischer, and T. Speck, From scalar to polar active matter: Connecting simulations with mean-field theory, Phys. Rev. E **101**, 022602 (2020).

[63] R. Großmann, I. S. Aranson, and F. Peruani, A particle-field approach bridges phase separation and collective motion in active matter, Nat. Commun. **11**, 5365 (2020).

[64] F. Peruani, T. Klauss, A. Deutsch, and A. Voss-Boehme, Traffic Jams, Gliders, and Bands in the Quest for Collective Motion of Self-Propelled Particles, Phys. Rev. Lett. **106**, 128101 (2011).

[65] F. D. C. Farrell, M. C. Marchetti, D. Marenduzzo, and J. Tailleur, Pattern Formation in Self-Propelled Particles with Density-Dependent Motility, Phys. Rev. Lett. **108**, 248101 (2012).

[66] J. Barré, R. Chétrite, M. Muratori, and F. Peruani, Motility-induced phase separation of active particles in the presence of velocity alignment, Rev. Mod. Phys **158**, 589 (2015).

[67] A. Martín-Gómez, D. Levis, A. Díaz-Guilera, and I. Pagonabarraga, Collective motion of active Brownian particles with polar alignment, Soft Matter **14**, 2610 (2018).

[68] E. Sesé-Sansa, I. Pagonabarraga, and D. Levis, Velocity Alignment Promotes Motility-Induced Phase Separation, Europhys. Lett. **124**, 30004 (2018).

[69] M. N. van der Linden, L. C. Alexander, D. G. A. L. Aarts, and O. Dauchot, Interrupted Motility Induced Phase Separation in Aligning Active Colloids, Phys. Rev. Lett. **123**, 098001 (2019).

[70] V. M. Worlitzer, G. Ariel, A. Be'er, H. Stark, M. Bär, and S. Heidenreich, Motility-induced clustering and meso-scale turbulence in active polar fluids, New J. Phys. **23**, 033012 (2021).

[71] B. Bhattacherjee and D. Chaudhuri, Re-entrant phase separation in nematically aligning active polar particles, Soft Matter **15**, 8483 (2019).

[72] J. Zhang, R. Alert, J. Yan, N. S. Wingreen, and S. Granick, Active phase separation by turning towards regions of higher density, Nat. Phys. **17**, 961 (2021).

[73] D. Andrienko, Introduction to liquid crystals, J. Mol. Liq. **267**, 520 (2018).

[74] P.-G. De Gennes and J. Prost, *The Physics of Liquid Crystals*, Vol. 83 (Oxford University Press, Oxford, UK, 1993).

[75] F. C. Poderoso, J. J. Arenzon, and Y. Levin, New Ordered Phases in a Class of Generalized *XY* Models, Phys. Rev. Lett. **106**, 067202 (2011).

[76] H. Chaté, F. Ginelli, and R. Montagne, Simple Model for Active Nematics: Quasi-Long-Range Order and Giant Fluctuations, Phys. Rev. Lett. **96**, 180602 (2006).

[77] J. Toner, Y. Tu, and S. Ramaswamy, Hydrodynamics and phases of flocks, Ann. Phys. **318**, 170 (2005).

[78] F. Peruani, A. Deutsch, and M. Bär, A mean-field theory for self-propelled particles interacting by velocity alignment mechanisms, Eur. Phys. J. Spec. Top. **157**, 111 (2008).

[79] H. Risken, *The Fokker-Planck Equation*, 2nd ed. (Springer, Berlin, 1996).

[80] J. Stenhammar, A. Tiribocchi, R. J. Allen, D. Marenduzzo, and M. E. Cates, Continuum Theory of Phase Separation Kinetics for Active Brownian Particles, Phys. Rev. Lett. **111**, 145702 (2013).

[81] B. Liebchen and D. Levis, Collective Behavior of Chiral Active Matter: Pattern Formation and Enhanced Flocking, Phys. Rev. Lett. **119**, 058002 (2017).

[82] D. Levis and B. Liebchen, Micro-flock patterns and macro-clusters in chiral active Brownian disks, J. Phys.: Condens. Matter **30**, 084001 (2018).

[83] G.-J. Liao and S. H. Klapp, Clustering and phase separation of circle swimmers dispersed in a monolayer, Soft Matter **14**, 7873 (2018).

[84] Z. Ma and R. Ni, Dynamical clustering interrupts motility induced phase separation in chiral active Brownian particles, arXiv:2104.11657 (2021).

[85] C. Reichhardt and C. J. Olson Reichhardt, Active matter transport and jamming on disordered landscapes, Phys. Rev. E **90**, 012701 (2014).

[86] T. Bhattacharjee and S. S. Datta, Confinement and activity regulate bacterial motion in porous media, Soft Matter **15**, 9920 (2019).

[87] A. Chardac, S. Shankar, M. C. Marchetti, and D. Bartolo, Emergence of dynamic vortex glasses in disordered polar active fluids, Proc. Natl. Acad. Sci. USA **118**, e2018218118 (2021).

[88] R. Matas-Navarro, R. Golestanian, T. B. Liverpool, and S. M. Fielding, Hydrodynamic suppression of phase separation in active suspensions, Phys. Rev. E **90**, 032304 (2014).

[89] N. Yoshinaga and T. B. Liverpool, Hydrodynamic interactions in dense active suspensions: From polar order to dynamical clusters, Phys. Rev. E **96**, 020603(R) (2017).

[90] G.-J. Liao, C. K. Hall, and S. H. Klapp, Dynamical self-assembly of dipolar active Brownian particles in two dimensions, Soft Matter **16**, 2208 (2020).